SUBMISSION TO:

Canadian Geotechnical Journal

DATE:

26 May 2014

TITLE:

Stability and failure mass of unsaturated heterogeneous slopes

AUTHORS:

Thi Minh Hue Le[1], Domenico Gallipoli[2], Marcelo Sanchez[3], Simon Wheeler[4]

AFFILIATIONS:

[1] SINTEF Buidling and Infrastructure, SINTEF, Grønnbygg, Rich. Birkelands vei 3, 7465 Trondheim, Norway. Tel: +47 (0) 9300 1834; Email: thi.le@sintef.no

[2] Laboratoire SIAME, Université de Pau et des Pays de l'Adour, Allée du Parc Montaury, 64600 Anglet, France; Tel : +33 (0)559574280; Email: domenico.gallipoli@univ-pau.fr

[3] Zachry Department of Civil Engineering, Texas A&M University, 3136 TAMU, College Station, TX 77843-3136, United States; Tel. (+1) -979- 862 6604; Fax: (+1) -979- 862 7696; Email: msanchez@civil.tamu.edu

[4] Infrastructure & Environment Research Division, School of Engineering, University of Glasgow, G12 8LT, Glasgow, United Kingdom; Tel: +44 (0)141 330 5201; Fax: +44 (0)141 330 4557; Email: Simon.Wheeler@glasgow.ac.uk

ABSTRACT:

Rainfall infiltration in an unsaturated soil slope induces loss of suction (and even positive pore-water pressures), which can eventually lead to failure. This paper investigates the probability and the size of failure of an unsaturated slope with spatially variable void ratio, subjected to a constant intensity rainfall. The random finite element method is employed in conjunction with a Monte Carlo simulation to stochastically evaluate the factor of safety and the size of the sliding mass. The results indicate that the mean value and the variability of these two quantities depend on both correlation length and coefficient of variation of the void ratio field. This dependency is more prominent during the transient regime than at steady states. Notably, the factor of safety in some cases can be low but the corresponding sliding mass is relatively small while, in other instances, the factor of safety might remain large though the associated sliding mass is very sizeable. The correlation between the factor of safety and the size of the sliding mass shifts from positive to negative as the rainfall progresses. A simple quadrant plot is suggested to assess the risk associated with slope failure taking into account both the factor of safety and the size of failure, rather than the factor of safety alone as it is usually the case. The study also demonstrates an application of a numerical approach to assess stability of geostructures composed of complex multiphase materials such as unsaturated soils or frozen soils.

KEY WORDS: heterogeneity, variability, unsaturated, slopes, rainfall, stochastic

INTRODUCTION

The effect of soil heterogeneity on slope stability has been stochastically studied over the last forty years by many authors, who have mainly assumed dry or fully saturated conditions (Alonso 1976; Babu and Mukesh 2004; Cho 2009; El-Ramly et al. 2002; El-Ramly et al. 2005; Fenton and Griffiths 2005; Griffiths and Fenton 2004; Griffiths et al. 2009; Griffiths et al. 2011; Hicks and Samy 2002; Hicks and Spencer 2010; Li and Lumb 1987; Low and Tang 1997; Matsuo and Kuroda 1974; Mostyn and Soo 1992; Mostyn and Li 1993). These studies mostly focused on the influence of shear strength on slope stability and have showed that the probability of failure increases with increasing coefficient of variation of shear strength (e.g. Griffiths and Fenton 2004). Some authors took into account the effect of spatial correlation and concluded that the assumption of an infinite correlation length (i.e. a homogeneous slope) led to conservative predictions of failure probability (Babu and Mukesh 2004; Mostyn and Soo 1992; Mostyn and Li 1993). Other authors (e.g. Griffiths and Fenton 2004; Griffiths et al. 2009) indicated instead that the assumption of an infinite correlation length for the undrained shear strength could lead to unconservative predictions of failure. The anisotropy of the correlation lengths was also investigated in some studies (e.g. Hicks and Samy 2002).

With reference to unsaturated conditions, previous research has been almost exclusively limited to homogeneous soils (Alonso et al. 1995; Ng and Shi 1998; Cho and Lee 2001; Tsaparas et al. 2002; Griffiths and Lu 2005; Lu and Godt 2008 and Gavin and Xue 2009). In spite of practical interest, very few studies have attempted to incorporate the variability of soil properties into the analysis of unsaturated slopes (e.g. Alonso and Lloret 1983; Arnold and Hicks 2010; Babu and Murthy 2005;

Cho 2014; Dou et al. 2014; Santoso et al. 2011b; Zhang et al. 2005; Zhang et al. 2014) mainly because of the high non-linearity of the problem. Zhang et al. (2005) analyzed the effect of the variation of hydraulic parameters and shear strength on the stability of an unsaturated slope during a rainstorm and showed that the coefficients of variation of both safety factor and displacement increase as the storm progresses. Their study took into account cross-correlations between soil properties but ignored spatial variability.

A few stochastic studies into rainfall-induced failure in unsaturated slopes published quite recently took into account spatial variability. The majority of these studies are however limited to infinite slopes with one-dimensional random variability of soil properties. Santoso et al. (2011b), for example, used subset simulation with a modified Metropolis-Hasting algorithm to estimate the probability of failure of an infinite unsaturated slope with randomly varied saturated permeability. Correlation length was found to cause deeper wetting fronts and higher negative heads at the layers above the wetting front during a rainstorm. This consequently led to lower probability of failure. Cho (2014) conducted a series of seepage and stability analyses of an infinite unsaturated slope during rainfall infiltration with randomly varying permeability. The author concluded, among other things, that the influence of the coefficient of variation and the correlation length of saturated permeability seemed to depend on the location of the critical failure surface (i.e. the surface with the lowest factor of safety). Dou et al. (2014) extended the Green-Ampt infiltration model and combined it with an infinite slope model to obtain a closed form of the limit state function. The Monte Carlo simulation method was then used to study the influence of saturated permeability on failure of an unsaturated slope during rainfall infiltration. Zhang et al. (2014) used a similar approach of combining the Green-Ampt model with the infinite slope model. The authors however varied both soil parameters and rainfall intensity-duration curves. Arnold and Hicks (2010) is one of the very few studies dealing with finite unsaturated slopes stochastically. The authors used the Bishop's effective stress approach (1959) to study the simultaneous variation of friction angle, cohesion, porosity, saturated permeability and air entry suction.

With respect to the extent of failure, some authors studied the depth of the sliding mass, but only qualitatively, to identify the factors that affect the depth of failure rather than quantifying the size of the sliding mass. Alonso and Lloret (1983) showed that the slope angle marking the transition from shallow to deep failures increase with soil dryness. Santoso et al. (2011) remarked that shallow failure mechanisms during rainfall infiltration in heterogeneous slopes of infinite length cannot be predicted using a homogeneous slope model. Hicks et al. (2008) presented a three-dimensional stochastic study of the size of the sliding mass in saturated slopes.

This study investigates the impact of the spatial heterogeneity of void ratio on the stability of an unsaturated slope subjected to rainfall infiltration via Monte-Carlo simulation. In particular, the random finite element method (Griffiths and Fenton 1993) is employed to stochastically evaluate the factor of safety and the extent of failure (quantified by the area of the sliding mass) at various times, during and after a rainfall. The study examines the sensitivity of the results to the coefficient of variation and correlation length of void ratio. The correlation between the factor of safety and the sliding area is explored using their joint probability distribution and a simple quadrant plot is suggested for risk assessment.

THE MODEL

Geometry and mesh discretisation

This study assumes a 10 m high slope of 2:1 gradient, which rests on a 20 m thick base and is discretized by a finite element mesh of 1515 quadrilateral elements (Fig.1). Finite element analyses are performed by using the software CODE_BRIGHT (UPC, 2010), which allows fully coupled thermo-hydro-mechanical simulations of boundary value problems in multiphase materials such as unsaturated soils and frozen soils.

The initial stress distribution is in equilibrium with gravity and is calculated by the software at the start of the analysis through the application of gravity to an initially weightless slope. The random variability of void ratio (e) is introduced before application of gravity to take into account the effect of the variation in soil unit weight (caused by the variability of e) on the initial stress distribution. The initial pore water pressures (p_w) are in hydrostatic equilibrium with the initial water table located 5 m below the slope toe. The pore air pressure is assumed constant and equal to zero (i.e. atmospheric), so that the suction s is equal to the negative value of pore water pressure, i.e. $s=-p_w$. The maximum initial suction is therefore attained at the crest of the slope AB and is equal to 150 kPa. This suction level falls in the lower end of the range observed in semiarid or arid environments such as, for example, in Australia (Cameron et al. 2006).

A mesh sensitivity analysis under saturated conditions showed that the assumed mesh produces reliable estimates of the factor of safety (Le 2011). The vast majority of elements are squares or parallelograms, each having an area of ~ 1 m^2. Approximately 1% of all elements, i.e. those in the centre of the mesh, have smaller areas than this value (Fig.1).

Simulation process

In the Monte Carlo analysis, each random finite element realization is analysed in two separate stages: i) an initial simulation of rainfall infiltration, up to a chosen time during or after the rainfall, to establish the stresses, strains and p_w inside the slope and ii) the subsequent application of the shear strength reduction technique (SRT) to calculate the factor of safety (*FoS*) and the area of the sliding mass (A_s) at that particular time.

In the first stage, a moderate constant rainfall of 43.2 mm/day over 10 days is simulated by imposing a "seepage" boundary condition on the ABCD surface (Fig.1). This boundary condition allows water to infiltrate into the soil at a constant rate as long as the p_w at the boundary is negative (i.e. existence of suction). If the p_w becomes equal or larger than zero, the boundary condition shifts to a constant $p_w = 0$ to avoid build-up of hydraulic head at ground surface. More detailed explanations of the seepage boundary condition can be found in CODE_BRIGHT Users' Manual (UPC 2010) or Le et al. (2012). After 10 days of rainfall, the simulation is continued for another 355 days (referred to as the post-infiltration period). Boundaries OA, OG and GD are assumed to be impermeable both during and after the rainfall. This causes the infiltrated water to accumulate inside the soil domain, hence raising the water table at the end of the rainfall. After day 10 (i.e. after the end of the rainfall), the boundary ABCD is assumed to be impermeable. Therefore, water loss from evaporation is prevented and any change of the *FoS* during the post-infiltration period is purely due to the redistribution of p_w. During the analysis carried out in this first stage, mechanical deformations are fully coupled with pore water flow, i.e. the equations of equilibrium and water flow are simultaneously solved in CODE_BRIGHT.

In the second stage, the FoS and A_s are evaluated at various times of interest by performing a separate SRT analysis at each of these times. Four times during the rainfall (0, 0.5, 5, 10 days) and four times during the post-infiltration period (15, 20, 100 and 365 days) are selected to capture the changes of the failure mechanism associated with a significant variation of the p_w field. In each SRT analysis the stresses and strains calculated during the first stage are imposed as initial conditions while the p_w is maintained fixed at every node. This means that, for example, to calculate the FoS and A_s after 5 days of rainfall, the SRT will be applied to a slope model with the starting stresses and strains equal to those obtained at day 5 during rainfall infiltration (calculated in the first stage). Moreover, as soil strength is reduced, the p_w remains fixed at every node and equal to the value calculated at day 5 during rainfall infiltration. The value of p_w is maintained fixed because the SRT analysis is purely a numerical technique to estimate the values of FoS and A_s corresponding to a given p_w field and does not simulate any physical phenomenon.

Hydraulic and mechanical constitutive relationships

The van Genuchten (1980) and van Genuchten and Nielsen (1985) models are used for the water retention curve and the permeability function, respectively, because they can realistically represent unsaturated soil behaviour in a simple and numerically stable way. These constitutive models are presented briefly below. More details about these relationships can be found in Le (2011); Le et al. (2012) and Le et al. (2013b):

$$S_e = \frac{S - S_r}{S_s - S_r} = \left(1 + \left(\frac{s}{s_e}\right)^{\frac{1}{1-m}}\right)^{-m} \qquad (1)$$

$$s_e = s_{eo} \exp(\eta(\phi_o - \phi)) \qquad (2)$$

$$k_s = k_{so} \frac{\phi^3}{(1-\phi)^2} \frac{(1-\phi_o)^2}{\phi_o^3} \qquad (3)$$

$$k_r = \sqrt{S_e}(1-(1-S_e^{1/m})^m)^2 \qquad (4)$$

$$\mathbf{q} = -k_s k_r \nabla\left(\frac{u_w}{\rho_w g} + z\right) \qquad (5)$$

The soil water retention curve (SWRC) van Genuchten (1980) is given by equation 1, which relates the effective degree of saturation (S_e) (calculated as a function of the current degree of saturation (S), the maximum degree of saturation (S_s), and the residual degree of saturation (S_r)) to suction s=-p_w through the air entry suction parameter s_e. In equation 2, the parameter s_e is in turn related to the porosity (ϕ) through parameter η which controls the rate at which s_e deviates from its reference value s_{eo} when ϕ deviates from its reference value ϕ_o (Roriguez et al. 2007 and Zandarin et al. 2009). Similarly, equation 3 describes the variation of the saturated permeability (k_s) from its reference value k_{so} when ϕ deviates from its reference value ϕ_o, as proposed by Kozeny (1927). Equation 4 describes the van Genuchten and Nielsen (1985) permeability curve linking the relative permeability k_r to the effective degree of saturation S_e through the parameter m, which can be geometrically interpreted as the curve gradient. The unsaturated permeability k_u is the product of the saturated and relative permeability (i.e. $k_u = k_s k_r$). In other words, the value of k_r is the normalised value of k_u to k_s. Finally, the unsaturated flow **q** is calculated using the generalized Darcy's law (equation 5). The symbols u_w, ρ_w, g and z indicate the pore water pressure, the water density, the gravitational acceleration and the elevation coordinate, respectively.

According to the above models, the heterogeneity of e, and hence of ϕ, influences the distribution of pore water pressure by influencing the SWRC (equations 1 and 2) and hence the k_r (equations 1, 2 and 4) and influencing the k_s through the Kozeny's equation (equation 3). The inclusion of the influence of randomly varying e on the SWRC and k_r, in addition to its influence on k_s, is a step-forward from existing probabilistic models considering similar effects. Phoon et al. (2010), for example, proposed a probabilistic model for the normalised SWRC. The author used a correlated lognormal vector containing the curve fitting parameters related to the shape and air entry value of the SWRC but did not take into account the variability of k_s. Santoso et al. (2011a) further developed the model proposed in Phoon et al. (2010) for the non-normalised SWRC in which the saturated water content is treated as a random variable. The Kozeny-Carman equation was also used by the authors to link random saturated water content to k_s. This approach implies that the variation of the SWRC and k_s are independent from one another, unlike in this study where they are related through the variation of e.

The values of all hydraulic parameters are summarized in Table 1. Note that the values of m, k_{so}, s_{eo} and η are assumed constant, spatially uniform and are taken around the middle of their typical range in order to avoid overly large or small values which can cause unrepresentative results (Bear, 1972; van Genuchten, 1980; Zandarin, 2009). In equation 1, the values of S_s and S_r are equal to 1 and 0.01, respectively.

A linear elastic model with an extended Mohr-Coulomb (MC) failure criterion (equation 6) describes the mechanical behavior of the unsaturated soil (Fredlund et al. 1978):

$$\tau = c' + \sigma \tan\phi' + s \tan\phi^b \qquad (6)$$

In equation 6, the shear stress at failure (τ) depends on the net normal stress (σ) and suction (s) through the friction angle (ϕ'), cohesion (c') and a parameter controlling the increase in shear strength with suction (ϕ^b). The component of strength contributed by suction (i.e. the 3rd term in equation 6) decreases with decreasing s and becomes zero for a fully saturated soil. The value of ϕ^b has been shown experimentally to increase with decreasing s (Escario and Saez 1986 and Gan et al 1988), approaching ϕ' in saturated conditions. The dependency between the angle ϕ^b and the suction is however not well-understood. Gan et al. (1988) suggested that the value of ϕ^b decreased to a relatively constant value as the soil desaturated to a higher matric suction. For simplicity, this study assumes a constant value for ϕ^b. The values of the strength parameters (c', ϕ' and ϕ^b) assumed in this study are typical of a clay and are based on the values reported by Bishop et al. (1960) for boulder clay and by Gan et al. (1988) for a compacted glacial till. The elastic parameter values, i.e. Young modulus (E) and Poisson ratio (ν), are also typical of a clay and chosen within their respective typical ranges of variation (Zhu 2014). The values of all mechanical parameters are summarized in Table 1.

In this study, the chosen value of $k_s = 10^{-5}$ m/s lies in the upper range of permeability for layered clay or silt with some clay. It is considered acceptable to adopt a value of k_s that is higher than the typical permeability of clayey materials due to the significant spatial variation of e. This spatial variation implies that the 'average' k_s would be elevated toward the upper values of the permeability range because, in heterogeneous soils, water follows preferential paths through more permeable areas, which has been shown in Le et al. (2012). The corresponding k_u is rather low, around 10^{-9}–10^{-10} m/s for $s \approx 150$ kPa which is found at the crest of the slope. The selection of a slightly elevated k_s also facilitates the numerical performance of the simulation by easing the steep transition in pore pressure across the wetting front formed during water migration through the slope domain.

In reality, the variation of porosity can also influence the values of mechanical parameters. In this study, however, it is assumed that porosity has no influence on the values of stiffness and strength, which are taken constant and spatially uniform. This assumption facilitates the investigation of the effect of the heterogeneity of porosity on the hydraulic behavior of the slope by isolating it from other effects. This study can however provide a reference for future research in which more complex probabilistic models, taking into account the influence of porosity on both hydraulic and mechanical parameters, can be adopted.

A non-associated flow rule with zero dilatancy is employed in the mechanical model, which means that no plastic volumetric strain occurs during yielding. A viscoplastic convergency algorithm is used to update the stress field during plastic loading.

SHEAR STRENGTH REDUCTION TECHNIQUE

One of the challenges in assessing slope stability by the SRT technique is to define failure based on the output of a finite element analysis. Detection of failure is normally associated either with the loss of global equilibrium or with the onset of a kinematic “sliding” mechanism. The former is identified by the “non-convergence” of the solution within a certain iteration ceiling (Griffiths and

Lane 1999; Zienkiewicz et al. 2005) while the latter relies on monitoring selected nodes to detect a sudden increase of displacements (Hicks and Spencer 2010).

The analysis of heterogeneous unsaturated slopes involves solving a complex system of coupled mechanical - hydraulic equations. Non-convergence can therefore be caused by a number of reasons that are unrelated to the loss of global equilibrium and, if counted as slope failure, can mislead risk assessment. Because of this, the current study adopted the displacement monitoring approach to detect slope failure. Those realizations, which did not converge due to reasons other than attainment of failure, were therefore disregarded. In heterogeneous slopes, the sliding mass might vary considerably in shape and size. The present study therefore takes a comprehensive approach by monitoring every node of the mesh to ensure that the occurrence of failure can always be detected and to estimate the size of the sliding mass. Failure is identified when one or more nodes satisfy a combination of criteria as discussed later.

In a saturated SRT analysis, the factor of safety (*FoS*) is defined as the factor by which the strength parameters (i.e. $\tan\phi'$ and c') must be divided to make a slope "barely stable" (Duncan 1996). In unsaturated soils, the extended Mohr-Coulomb criterion involves, in addition to ϕ' and c', an extra parameter ϕ^b which controls the expansion of the failure envelope with increasing suction. The product of suction and $\tan\phi^b$ contributes to shear strength in a similar way to cohesion and is often lumped with c' to create an "enhanced cohesion" term. It is therefore reasonable to apply the strength reduction factor to $\tan\phi^b$ in the same manner as to $\tan\phi'$ and c'. In this study, the *FoS* for unsaturated soil is therefore defined as:

$$FoS = \frac{c'_{actual}}{c'_{fail}} = \frac{\tan\phi'_{actual}}{\tan\phi'_{fail}} = \frac{\tan\phi^{b}_{actual}}{\tan\phi^{b}_{fail}} \quad (1)$$

During a SRT analysis, the response of the slope is monitored while the shear strength parameters are reduced by dividing them by a factor that is initially equal to one and is incremented by 0.01 in a number of consecutive steps. An initial validation of the SRT method is performed in this work for the simpler case of a homogeneous slope by comparing the *FoS* estimated as described above with that computed by the limit equilibrium method (LEM). The slope considered for this validation has the same geometry and dimension as shown in Fig.1 and the same hydraulic parameters as in Table 1. The void ratio is spatially uniform and equal to 0.5 (corresponding to the mean value of void ratio adopted in this study). The LEM estimation is performed by, first, using the software SEEPW (GEO-SLOPE International, Ltd, Alberta, Canada) to calculate the p_w distribution at different times during rainfall infiltration. The obtained p_w distribution is then fed into the software SLOPEW (GEO-SLOPE International, Ltd, Alberta, Canada) to estimate the corresponding *FoS* by the LEM. Figure 2 shows that the two methods produce remarkably similar trends of variation of *FoS* over time, though the *FoS* obtained by the LEM appears systematically higher than the *FoS* obtained by using the FEM (however the relative difference between the two curves is not significant). This discrepancy might be caused by various reasons, including the restriction imposed on the geometry of the failure surface in the LEM, the assumption about the forces acting between slope slices in the LEM and the coupling of hydraulic and mechanical behaviour during rainfall in the FEM but not in the LEM. In addition, there might be a slight variation in the p_w distribution predicted by SEEPW and CODE_BRIGHT due to the different meshes used in the two cases.

RANDOM VOID RATIO FIELD

In unsaturated soils, the wetting process can lead to a drop in suction and even to positive p_w, which reduces shear strength and contributes to the loss of stability. In this study, the computed slip surfaces tend to cut mainly through the unsaturated region. This implies that the suction drop in the unsaturated region plays a more relevant role than the build-up of positive p_w in the saturated region. Due to the spatial variation of e, the advancing wetting front during rainfall is uneven and geometrically irregular, unlike the smooth and uniform wetting front observed in homogeneous soils (Le et al. 2012). This is because, in heterogeneous soils, water follows preferential paths causing an uneven suction reduction over the soil domain. Soil elements experiencing large suction drops might reach failure earlier or under lower stresses than neighbouring elements experiencing smaller reductions of suction. Therefore, the heterogeneity of e can change the failure mechanism compared to the case of a homogeneous soil, as the slip surfaces passing through the weaker, "wetter" elements tend to result in lower *FoS*.

In this study, the mean of the void ratio field $\mu(e)$ is kept constant at 0.5 for all simulations while five values of the coefficient of variation (i.e. $COV_e = 0.1$, 0.2, 0.4, 0.8 and 1.6), and five values of the correlation lengths in both horizontal and vertical directions (i.e. $\theta_h(e)= \theta_v(e)= \theta(e) = 2$, 4, 8, 16 and 32 m) are investigated. Baecher and Christian (2003) compiled data from various sources and suggested a range of 0.13 – 0.42 for the COV_e while ranges of 0.07 – 0.3 and of 0.15 – 0.3 have been suggested by Lacasse and Nadim (1996) and Lumb (1974), respectively. Santoso et al. (2011a) used a value of $COV_e = 0.13$ for sandy clay loam and loam based on the volumetric water content from test data provided in the unsaturated soil database - UNSODA (Leij et al. 1996). Le et al.

(2013a) reported a range of COV_e from 0.05 to 0.26 for porosity of various soils including glacial clays, sands and chalks. The two upper values of COV_e considered in this study are much larger than the coefficients of variation reported in the literature. The two large values of COV_e (in addition to the usual values of 0.1, 0.2 and 0.4) are chosen in order to emphasize the effect of the variation of e on unsaturated slopes. In addition, they might be more representative of the variability of compacted soils, such as embankment fills, which can be composed of mixed materials from various sources leading to very large variations in void sizes. With respect to correlation length, there are few published values from real measurements for e. Onyejekwe and Ge (2013) analysed the data for fined grain soils at four different locations in Missouri from 11 CPTu soundings together with laboratory tests from 15 different boreholes and reported values of $\theta_v(e)$ between 0.55 to 4.66 m. Phoon et al. (2006) suggested $\theta_v(e) \approx 3$ m for organic silty clay. The values of $\theta_h(e)$ are often much larger than the $\theta_v(e)$ (Phoon and Kulhawy 1999). Given this limited information, the selection of a lower bound of $\theta(e) = 2$ m for this study is considered practically reasonable.

To examine the possible values of degree of saturation and unsaturated permeability modelled by equation 1 to 5, Figure 3 presents the variation of the soil water retention curve and the unsaturated permeability curve with porosity (and hence, void ratio) over a suction range from 1 to 1000 kPa which is relevant for this study. Five values of porosity from 0.1 to 0.7 are considered. A value of porosity larger than 0.7 or smaller than 0.1 is quite unlikely for the range of input coefficient of variation adopted in this study. As can be seen from Figure 3, at $s \approx 150$ kPa at the crest of the slope, the soil would be from 50 to 80% saturated and have a corresponding k_u of around $10^{-10} - 10^{-9}$ m/s. Noticeably, the degree of saturation tends to decrease with increasing porosity while the k_u at the suction range larger than 20 kPa no longer increases with larger porosity (Fig. 3a). This implies that the areas with larger porosity/void ratio are not always the most permeable areas in unsaturated soils as it is the case for saturated soils.

The selection of the mesh size in this study aims at balancing between capturing the soil variability and avoiding excessive computational expenses which is critical for Monte Carlo simulation. The selected mesh of 1m x 1m is considered reasonable for this study because it allows the Monte Carlo analyses to be performed within an acceptable amount of time. In addition, the element size is smaller than the lowest $\theta(e)$ = 2 m, which means the soil variability can be reasonably reflected because the impact of local averaging over the area of each element is minimal. Figure 3b shows that, at high suction (above 100 kPa), the k_u becomes quite low (< 10^{-9} m/s) and less varied among different porosities.

In the following, the random field of e is assumed to be isotropic (i.e. ratio of horizontal over vertical correlation length $\alpha = \theta_h(e)/\theta_v(e) = 1$), unless otherwise specified. Therefore, in an isotropic field, the symbol $\theta(e)$ will be used to indicate the same correlation length in both vertical and horizontal directions. Mapping of the random field onto the finite element mesh is achieved by allocating to each element the random value with coordinates that are closest to the centroid of the element (Le 2011; Le et al. 2012).

Although the void ratio can theoretically be any positive value, most soils are likely to have a minimum and a maximum e. Fenton and Griffiths (2008) suggested that perhaps a bounded tanh type distribution would be the most appropriate for e variability. This type of distribution is however hard to defined because it requires 4 soil parameters. A number of authors suggest a log-normal or normal distribution for the variation of e because of their simplicity and popularity (Baecher and Christian 2003, Laccasse and Nadim 1996). With proper selection of mean and standard deviation, a normal or log-normal distribution yields very small possibilities of generating excessively inappropriate values. Therefore, the normal and log-normal distributions are generally regarded as suitable for void ratio/porosity of materials. A log-normal distribution is selected in this study because it ensures that the value of *e* is always positive, and hence the corresponding value of porosity stays between 0 and 1.

FACTOR OF SAFETY AND AREA OF SLIDING MASS

Numerous realizations are required for each Monte-Carlo simulation, so it is not possible to identify slope failure by manually examining individual simulations. Appropriate criteria are therefore defined so that failure can be automatically identified by using a numerical algorithm. In particular, failure is recorded when the following three criteria are simultaneously satisfied at one node on the exposed boundary of the finite element mesh (i.e. boundary ABCD in Fig. 1):

i. Increment of vertical or horizontal displacement increases by more than 10 times in one strength reduction step (i.e. when the strength reduction factor is increased by 0.01).
ii. Increment of total displacement increases by more than 2 mm in one strength reduction step.
iii. Cumulative vertical or horizontal displacements are larger than 10 mm.

These criteria were established after examination of the displacement fields in a large number of realizations. Criterion (i) identifies the sudden increase in vertical or horizontal displacement rate at a given node, which is the fundamental condition for detecting failure. However, criterion (i) alone might be misleading because a displacement increment that is very small in absolute terms can still be more than 10 times larger than the displacement increment observed during the previous strength reduction step. This might, for example, be the consequence of numerical oscillations rather than slope failure. An additional criterion (ii) is therefore required to ensure that the displacement increment is substantial and hence indicative of failure. Criterion (ii) alone is also not sufficient because it can be satisfied by a node experiencing rather large displacement increments in subsequent strength reduction steps, even without the occurrence of overall failure. Finally, criterion (iii) needs to be simultaneously satisfied to ensure that the slide has moved by a considerable amount, which signifies the initiation of a mechanism rather than an occasional large displacement at one node.

In each realization, the *FoS* is recorded as the smallest strength reduction factor at which criteria (i), (ii) and (iii) are simultaneously satisfied by at least one node on the exposed boundary of the finite element mesh. This *FoS* marks the evolution of failure from unconnected regions inside the soil domain to a continuous band that causes sliding.

In a conventional slope stability study, risk assessment is normally based on likelihood of failure, which is in turn linked to the *FoS*. However, a large sliding mass is more likely to cause extensive damage and poses a greater hazard than a shallow slide, even if the former has a higher *FoS* than the latter. Therefore, a better estimate of risk should take into account both the likelihood and the size of failure. The algorithm used to monitor displacements is also employed in this study to estimate the size of failure. After identifying the first node on the exposed boundary of the mesh that satisfy criteria (i), (ii) and (iii) simultaneously (which occurs for a strength reduction factor equal to the

FoS), the SRT analysis is continued until it can no longer progress (i.e. due to excessively large displacements). This is to allow the sliding mass to develop and move substantially. At the end of each SRT analysis, the number of nodes over the entire mesh satisfying criteria (i), (ii) and (iii) is recorded and assumed to be equal to the area of the sliding mass (A_s). The fulfillment of the above three criteria implies that the corresponding node is located on the sliding mass (though different nodes inside the mass might fulfill the criteria at different values of the strength reduction factor during the SRT analysis). The above approximation of A_s is based on the observation that each node identifies an area made up of the sum of one quarter from each of the four elements sharing that node. Since the mesh mostly consists of square or parallelogram elements of 1 m^2, the area allocated to each node is also approximately equal to 1 m^2. In reality, the number of nodes slightly over-estimates the value of A_s as nodes located on or next to the boundaries of the sliding mass should be allocated smaller areas. Nevertheless, the variation of A_s is reasonably described by the variation of the number of nodes that satisfy the above failure criteria because, if A_s increases, the number of nodes located on the sliding mass also increases in an almost proportional fashion and vice versa. Given that this study focuses on investigating the sensitivity of failure to different parameters, the above approximation of A_s is considered satisfactory. For investigations of real slopes, it is recommended that A_s is estimated more accurately either by using a finer mesh or by directly measuring the area contained inside the slip surface.

QUALITATIVE ASSESSMENT AND CASES EXAMINATION

Figure 4 shows a sample distribution of ϕ mapped onto the finite element mesh in Fig. 1. This distribution corresponds to a random field of e with $\mu(e)$ = 0.5, COV_e = 0.8 and $\theta(e)$ = 8 m. Porosity

(ϕ), rather than void ratio (e), is plotted because the value of ϕ is bound between 0 and 1, which facilitates visual presentation of the random field by avoiding an extremely large range of numerical values. In this example, since the value of COV_e is large, the range of ϕ becomes relatively large for a domain of the size considered here (it varies from 0.05 to 0.75 in Fig. 4). This is however considered preferable for illustrative purposes in order to emphasize the effect of soil heterogeneity on the computed results.

Note that this study ignores the decrease of ϕ with depth due to increasing overburden pressure because of the relatively small height of the slope ($\leq$ 30 m). The significance of this assumption was evaluated by application of gravity to a homogeneous slope of the same dimensions to those used in the present study, which yielded a negligible variation of ϕ (i.e. less than 0.003 difference between the top and bottom boundaries of the mesh) compared to the degree of variability introduced by the random field.

Figure 5 shows the vertical displacement recorded at point A of the mesh (Fig. 4) during the SRT analyses undertaken at different times. Displacements increase significantly once failure occurs (Fig. 5). In addition, the *FoS* decreases during the rainfall but increases back once the rainfall stops (and stabilizes around 1.39 after 100 days for this particular realization).

Figure 6 demonstrates that the heterogeneous porosity field produces an "uneven" distribution of p_w during the rainfall and until the early stages of the post-infiltration period (i.e. until day 20). At the start of the rainfall (0 – 0.5 days), the *FoS* and A_s attain their largest values because no or little wetting of the slope face has occurred. For this realization, the A_s is smallest at an intermediate time during the rainfall (day 5) because, after 5 days of infiltration, the superficial soil layer has been weakened enough to induce a shallow failure mechanism confined to the wetted soil region (Fig. 6c). Therefore, the sliding mass at day 5 is smaller than at any other time (Fig. 6). On the other hand, the *FoS* drops to the lowest value at the end of the rainfall (10 days) due to suction loss in the unsaturated zone and water table rise in the saturated zone (Fig. 6d). After the rainfall, the *FoS* increases back due to the recovery of suction in the soil region close to the slope face (Figs. 6e-h) but it does not attain the same value as at day 0 due to accumulation of water (i.e. water table rise) inside the soil domain caused by the impermeable vertical and bottom boundaries. Finally, the higher hydrostatic water table at the end of the simulation than at the start also produces smaller A_s at the end of the simulation than at the start (Figs. 6a and h). It is important to note that only the initial sliding is detected in this study at each rainfall time while progressive failure is not accounted for.

STATISTICAL CHARACTERISATIONS

The reliability of the statistics of *FoS* and A_s is assessed by plotting the running means $\mu(FoS)$ and $\mu(A_s)$ together with their corresponding 95% confidence intervals against the number of realizations N (e.g. Fig. 7). Figure 7 indicates that the values of $\mu(FoS)$ and $\mu(A_s)$ converge rather quickly, i.e. after around 60 realizations at 5 days of rainfall. At this point, the 95% confidence interval of *FoS* and A_s becomes relatively narrow indicating stabilization of the standard deviation of the *FoS* $\sigma(FoS)$. The *FoS* of individual realisations ranges over a wider interval at day 5 (≈1 to 2.2) than at day 0 (≈1.6 to 2.2) (Fig. 7 a and b). This is caused by the more significant differences in the suction and stresses distributions of distinct realizations at day 5 compared to day 0. At other times, the convergence of the statistics of *FoS* is achieved with a smaller number of realizations than 60. The value of A_s spans a wide range and, at intermediate rainfall times (e.g. 5 days), exhibit skewness with dominance of relatively small values and a mean $\mu(A_s)$ higher than the majority of realizations.

Several probability distributions functions (pdf) were initially fitted to the frequency histograms of *FoS* and A_s and, most of the times, the log-normal function was found to provide a simple and acceptable representation in both cases (e.g. Fig. 8). Figure 8 indicates that the fit of the log-normal pdf to the A_s histogram is worst at day 5, which is due to the pronounced skewness of the data and large variability at this particular time as explained earlier (Fig. 7d). The match between the fitted log-normal pdfs and the corresponding histograms at 0.5 day, 15 days, 100 days and 365 days (not shown in Fig. 8) are generally similar to the match at 0 day, 10 days, 20 days and 100 days, respectively. The fitted log-normal pdfs are used in later sections to estimate the probability of failure and to construct the joint probability distribution between *FoS* and A_s in order to assess their correlation.

INFLUENCE OF VARIABILITY CHARACTERISTICS OF VOID RATIO

Factor of Safety and probability of failure

The changes of the mean and coefficient of variation of the factor of safety, $\mu(FoS)$ and COV_{FoS}, over time follow very similar patterns for different values of COV_e, $\theta(e)$ and α (i.e. anisotropy of correlation length) as shown in Figure 9. As water infiltrates, the $\mu(FoS)$ decreases and attains a minimum at 10 days, just before rainfall stops. This is due to the strength reduction caused mainly by the suction loss in the unsaturated region and, to a lesser degree, by the positive p_w rise in the saturated region. From day 10 to 365, infiltration is no longer occurring leading to the recovery of $\mu(FoS)$ to a value that is however smaller than the one prior to rainfall because of the rise of water table. The COV_{FoS} changes marginally up to 0.5 days, then it increases considerably from 0.5 to 5 days due to the larger variability in the suction distribution within the soil domain. The COV_{FoS} peaks at day 5 (except for COV_e = 0.1) but then decreases from day 5 to day 15 and fluctuates within a small range after that.

As the variability of *e* increases with increasing values of the COV_e, the heterogeneity of permeability, porosity and degree of saturation also becomes larger. The larger heterogeneity of permeability then increases the variability of suction over the soil domain, while the larger heterogeneity of porosity and degree of saturation increases the variability of the soil unit weight and, hence, of stresses. The "weakest" slip surface (which governs the *FoS*) tend to occur in regions of low strength. As the suction and stresses become more variable, the lower bound of soil strength decreases. Therefore, an increase of COV_e tends to cause a decrease of $\mu(FoS)$ (at times before 100 days) and an increase of COV_{FoS} (Figs. 9a and b).

As $\theta(e)$ increases from 2 to 32 m (with α=1), the $\mu(FoS)$ changes marginally up to day 20 but exhibits minor increases with higher values of $\theta(e)$ from day 20 onward (Fig. 9c). At the same time, the COV_{FoS} increases considerably (Fig. 9d). This is because 'regions of strongly correlated *e*' (referred, in short, as "regions" later on) increase in size with larger $\theta(e)$, which reduces the average number of such "regions" that the slip surfaces pass through. For example, a 12 m long slip surface might pass through, on average, 6 "regions" in a domain with $\theta(e)$ = 2 m, but can be contained within one single "region" in a domain with $\theta(e)$ > 12 m. The decreasing number of "regions" cut by the slip surfaces increases the variation of average soil strength along the slip surfaces between realizations because there is less compensating effects between 'weak' and 'strong' regions. This leads to an increase of the COV_{FoS} with increasing $\theta(e)$. Another factor is that the number of independent realisations (i.e. realisations with zero correlation with one another) tends to decrease statistically with increasing $\theta(e)$ which also contributes to increasing COV_{FoS} (Fenton and Griffiths 2008).

The influence of anisotropy of correlation lengths (α) is also investigated by keeping the horizontal correlation length $\theta_h(e)$ constant while reducing the vertical correlation length $\theta_v(e)$. Two values of $\theta_h(e)$ = 8 and 16 m are considered. For each $\theta_h(e)$, the $\theta_v(e)$ is scaled down by an anisotropic ratio ($\alpha = \theta_h(e)/\theta_v(e)$) equal to 2, 4 and 8. This implies that the "regions" become increasingly 'compressed' vertically and, hence, have a more elongated shape in the horizontal direction. The similarity in variation patterns of $\mu(FoS)$ and COV_{FoS} with decreasing $\theta(e)$ (Figs. 9c and d) and with increasing α (Figs. 9e and f) suggests that the effect of the decreasing size of the "regions" dominates over the effect of the more elongated shape. The former is caused by the proportional decreases in both $\theta_v(e)$ and $\theta_h(e)$ at the same time, hence changing the size but not the shape of the "regions"; while the latter corresponds to a decrease in $\theta_v(e)$ while $\theta_h(e)$ stays constant, hence changing both size and shape of the "regions". For the range α investigated, the change in shape alone appears to have minimal influence on the variation of $\mu(FoS)$ and COV_{FoS}.

The probabilities of failure P_f presented in Fig. 10 for isotropic soils (i.e. α=1) are calculated by assuming a log-normal probability distribution of the FoS. To facilitate presentation, the vertical scale in Fig. 10 is set from 10^{-10} to 1 and hence data points corresponding to insignificant probabilities ($P_f < 10^{-10}$ at low COV_e and $\theta(e)$ or at times before day 5) do not appear in Fig. 10. From day 5, the value of P_f increases significantly with increasing COV_e or $\theta(e)$. The highest P_f occurs at day 10 indicating that the drop in $\mu(FoS)$ at day 10 (Figs. 9a and c) has a dominant effect over the increase in COV_{FoS} at day 5 (Figs. 9b and d). The interacting trends of time and heterogeneity, as featured in Fig. 10, highlight the complexity and the importance of taking into account both factors in assessing the failure probability of unsaturated slopes during rainfall.

Size of sliding area

The variation of the mean and coefficient of variation of the sliding area, $\mu(A_s)$ and COV_{As}, over time for different values of COV_e, $\theta(e)$ and α are very similar (Fig. 11). The $\mu(A_s)$ becomes minimum at a rainfall time of 5 – 10 days, then increases back after the rainfall stops at day 10. The value of COV_{As} fluctuates around a relatively low value during the first half day of rainfall but then increases sharply and attains a maximum at day 5 for all values of COV_e, followed by a decrease to a stable value from day 20 onward.

Increasing heterogeneity (i.e. larger COV_e) causes larger variation in A_s which leads a considerable increase of COV_{As} (Fig. 11b). It also appears that as the “regions” of correlated *e* become larger (i.e. with increasing $\theta(e)$ or decreasing α) the size of the sliding mass also becomes more variable between realizations leading to generally higher COV_{As} (Figs. 11d and f).

Correlation between Factor of Safety and size of sliding mass

The correlation between the stochastic data of *FoS* and of A_s is examined by constructing the bivariate normal distribution of the natural logarithms of *FoS* and A_s because both these quantities can be reasonably assumed to follow normal distributions. Figures 12 and 13 show the individual realisations together with the contour ellipses from the joint probability distributions on a log-log scale. The contours correspond to probabilities equal to 10, 30, 50, 70 and 90% (i.e. each contour encircles an area where the probability of a realisation falling outside the area is equal to the probability represented by the contour).

There seems to be little correlation between ln*FoS* and lnA_s at the start (0 – 0.5 days) and at the end (100 – 365 days) of the simulation, when the suction distribution can be considered to be almost hydrostatic. This is evident from the very small slopes of the major axis of the contour ellipses (Figs. 12 and 13). As the rainfall progresses, there appears to be a linear correlation between ln*FoS* and lnA_s, which is positive at day 5, as indicated by positive slopes of the major axes of the ellipses. The correlation changes to negative at day 10, as shown by negative slopes, and the degree of correlation decreases from day 10 to day 20 (Figs. 12 and 13) as the suction distribution within the soil domain tends again towards hydrostatic. The results presented in Figures 12 and 13 correspond to an isotropic random field with $\mu(e)$ = 0.5, COV_e = 0.8 and $\theta(e)$ = 8 m but similar variation patterns are observed for other input values of COV_e, $\theta(e)$ and α.

Figure 12 shows that the realisations at day 5 appear to concentrate in two distinct areas. A large number of realizations are located in the region of low *FoS*/small A_s while a relatively small number of realizations occupy the region of high *FoS*/large A_s. This separation is due to the existence of a ‘critical’ depth determining the failure mechanism. With increasing e and hence larger ϕ, the saturated permeability k_s becomes higher following Kozeny's relationship (equation 3). Conversely, the relative permeability k_r becomes lower according to the permeability function (equation 4) due to lower values of the effective degree of saturation S_e. This is because, with larger ϕ, it becomes easier for the air to enter the soil voids (i.e. parameter s_e controlling the air entry value of soil decreases in equation 2) while, at the same time, the same amount of water occupies a smaller proportion of void (i.e. a decrease in S_e as in equation 1). The unsaturated permeability is the product of k_s and k_r can decrease or increase with ϕ depending on the magnitude of suction. More detailed discussion about changes of unsaturated permeability with ϕ can be found in Le (2011). In this study, the suction range is relatively low (< 150 kPa), which means that the unsaturated permeability tends to decrease with increasing ϕ or e. In those realizations characterized by high values of e at the slope face such as in Fig. 14a, the low unsaturated permeability inhibits water flow leading to a shallow infiltration depth (Fig. 14c). In such cases, the slip surface tends to cut though the deep unsaturated soil region leading to large values of A_s and FoS (Fig. 14c). Conversely, if the rainfall has infiltrated beyond this critical depth, the failure slip tends to be confined within the wetted superficial soil region leading to small values of A_s and FoS (e.g Figs. 14b and d).

The existence of correlation between lnFoS and lnA_s observed in Figs. 12 and 13 suggests a possible simple risk assessment method for slope stability, taking into account both the probability of failure and the size of failure. In Fig. 15, the FoS-A_s plane is divided into four quadrants by a vertical line at a limit state A_{sL} and a horizontal line at a limit state FoS_L. A slope is considered to be risky due to either low FoS (i.e. $FoS < FoS_L$ and hence the realization locates below the FoS_L) or large A_s (i.e. $A_s > A_{sL}$ and hence the realization locates to the right of the A_{sL}). This method of assessing risk is referred to as the ‘quadrant plot’ in this study.

The limit state values should be set depending on the required slope performance, taking into account both the probability/scale of failure and the consequences of failure. For example, a slope near a school will require a very high limiting value for *FoS* and a very low limiting value for A_s, while, for a subsea slope, it is likely to be acceptable to set a medium limiting value for *FoS* and a rather high limiting value for A_s. For illustration purpose, the FoS_L and A_{sL} are set at 1.4 and 100 m^2 respectively in this study, based on experience from the stability study of an actual railway embankment (Fig. 15). The four quadrants are then rated as Low Risk (LR) for the case with a low A_s/high *FoS* combination, Medium Risk (MR) for the cases with either a high A_s/high *FoS* or a low A_s/low *FoS* combination, and High Risk (HR) for the case with a high A_s/high *FoS* combination.

The contours corresponding to a 10% probability of a realisation falling outside the encircled area (for COV_e = 0.8 and $\theta(e)$ = 8 m) are shown, for different times, in Fig. 15 to illustrate the application of the quadrant plot method. For the limit values chosen in this study, this specific slope has a MR rating at the beginning of the rainfall (i.e. 0 – 0.5 day), with the risk being dominated by large failures. As rainfall infiltration progresses to day 5, the risk spread to all quadrants, including the high risk region (HR), due to the large variation in both *FoS* and A_s (and the consequent expansion of the 10% probability ellipse). The positive correlation at day 5 indicates that A_s tends to be larger as *FoS* increases, and hence MR is the prevalent rating, with either high *FoS* but large A_s or low *FoS* but small A_s. The shift to a negative correlation from day 10 indicates that there is potentially a higher probability of slope realizations falling inside the HR rating quadrant.

The application of the quadrant plot method shows that combining both *FoS* and A_s in evaluating slope stability can lead to a more informative assessment of the risk than when using the probability of failure alone.

CONCLUSIONS

This paper investigated the effect of randomly heterogeneous void ratio on the risk assessment of an unsaturated slope subjected to rainfall infiltration via Monte Carlo simulation. Simulations were conducted over a rainfall infiltration period (day 0 to 10) and a post-infiltration period after the rainfall has stopped (day 10 to 365). Factor of safety and size of failure (represented by the area of sliding mass) were estimated at 4 times during the rainfall and 4 times after the rainfall. The increasing loss of shear strength provided by suction during rainfall infiltration causes a decrease of the mean factor of safety and a wider variation of the factor of safety for individual realizations. The mean factor of safety attains a minimum at the end of the rainfall (day 10) while the coefficient of variation reaches a maximum at an intermediate rainfall time (around day 5). Over the post-infiltration period, the suction distribution increasingly stabilises towards a new hydrostatic steady state and hence both the mean and the coefficient of variation of factor of safety become increasingly constant.

The variations over time of the mean and coefficient of variation of the sliding area follow very similar patterns to the mean and coefficient of variation of the factor of safety, respectively. Increase in soil variability and expansion of correlated region (corresponding to increasing coefficient of variation and correlation length of the input random void ratio, respectively) cause only slight changes in the mean but significant increases in the coefficient of variation of both factor of safety and sliding area. The anisotropy of correlation length α in the range from 2 to 8 is also investigated but found to have marginal influence.

The log-normal distribution function is found to capture acceptably well the distribution of the factor of safety and the sliding area at various times during the simulation period. Assuming a log-normal distribution for the factor of safety, the estimated probability of failure reaches the highest value at the end of the rainfall (10 days). The probability of failure also consistently increases as the soil void ratio becomes more variable and correlated over a longer distance due to the widening of the variation range of the factor of safety.

The bivariate normal distribution reveals a positive correlation between the factor of safety and the sliding area at intermediate time (day 5) which shifts to negative at the end of the rainfall (day 10). This correlation does not seem to exist when the suction distribution is close or at a steady state (i.e. hydrostatic) either at the beginning of the rainfall (0 – 0.5 days) or long after the rainfall has stopped (after day 100). A simple quadrant plot is suggested, which divides the space of factor of safety –sliding area into low, medium and high risk regions based on their limit state values. The plot allows assessing the risk of slope failure in a more intuitive way by taking into account not only the probability of failure but also the scale of the failure mass.

Further study should concentrate on verifying the correlation between the factor of safety and the size of failure based on real data on slope failures. The approach of assessing stability demonstrated in this study is useful for geostructures composed of multiphase materials and can also be extended from unsaturated soils to other complex soils such as frozen (unsaturated) soils in permafrost areas.

ACKNOWLEDGEMENTS

This research has been supported by the centre for research-based innovation, Sustainable Arctic Marine and Coastal Technology (SAMCoT), and the Scottish Funding Council through the Glasgow Research Partnership in Engineering (GRPE).

REFERENCES

Alonso, E.E. 1976. Risk analysis of slopes and its application to Canadian sensitive clays. Géotechnique **26**(3): 453-472.

Alonso, E.E., Gens, A., Lloret, A., and Delahaye, C. 1995. Effects of rainfall infiltration on the stability of slopes. *In* Proceedings Of The First International Conference On Unsaturated Soil (6-8 September 1995). *Edited by* E. Alonso and P. Delage. Balkema, Paris, France.

Alonso, E.E., and Lloret, A. 1983. Evolution in time of the reliability of slope in partially saturated soils. *In* Fourth International Conference on Application of Statistics and Probability in Soil and Structural Engineering *Edited by* E. Pitagora, Bologna, Italy. pp. 1363-1376.

Arnold, P., and Hicks, M.A. 2010. Stochastic modelling of unsaturated slope stability. *In* Fifth International Conference on Unsaturated Soils. *Edited by* E. Alonso and A. Gens. CRC Press/ Balkema, Barcelona, Spain. pp. 1237-1242.

Babu, G.L.S., and Mukesh, M.D. 2004. Effect of soil variability on reliability of soil slopes. Géotechnique **54**(5): 335-337.

Babu, G.L.S., and Murthy, D.S.N. 2005. Reliability analysis of unsaturated soil slopes. Journal of Geotechnical and Geoenvironmental Engineering **131**(11): 1423-1428. doi: 10.1061/(asce)1090-0241(2005)131:11(1423).

Baecher, G.B., and Christian, J.T. 2003. Reliability and statistics in geotechnical engineering. Wiley, Chichester, United Kingdom.

Bear, J. 1972. Dynamics of Fluids in Porous Media. Dover.

Bishop, A.W. 1959. The principle of effective stress. Tecnisk Ukeblad **39**: 859 - 863.

Bishop, A.W., Alpan, I., Blight, G.E., and Donald, I.B. 1960. Factors controlling the strength of partly saturated cohesive soils. *In* Regional Conference on Shear Strength of Cohesive Soils, Boulder. pp. 503-532.

Cameron, D.A., Jaksa, M.B., Wayne, P., and O'Malley, A. 2006. Influence of trees on expansive soils in southern Australia. *In* Expansive soils: recent advances in characterization and treatment. *Edited by* A.A. Al-Rawas and M.F.A. Goosen. Taylor & Francis, London, UK. p. 526.

Cho, S.E. 2009. Probabilistic stability analyses of slopes using the ANN-based response surface. Computers and Geotechnics **36**: 787-797.

Cho, S.E. 2014. Probabilistic stability analysis of rainfall-induced landslides considering spatial variability of permeability. Engineering Geology **171**(0): 11-20. doi: http://dx.doi.org/10.1016/j.enggeo.2013.12.015.

Cho, S.E., and Lee, S.R. 2001. Instability of unsaturated soil slopes due to infiltration. Computers and Geotechnics **28**(3): 185-208.

Dou, H.-q., Han, T.-c., Gong, X.-n., and Zhang, J. 2014. Probabilistic slope stability analysis considering the variability of hydraulic conductivity under rainfall infiltration–redistribution conditions. Engineering Geology **183**(0): 1-13. doi: http://dx.doi.org/10.1016/j.enggeo.2014.09.005.

Duncan, J.M. 1996. State of the art: Limit equilibrium and Finite-element analysis of slopes. Journal of Geotechnical and Geoenvironmental Engineering **122**(7): 577-596.

El-Ramly, H., Morgenstern, N., and Cruden, D.M. 2002. Probabilistic slope stability analysis for practice. Canadian Geotechnical Journal **39**: 665-683.

El-Ramly, H., Morgenstern, N.R., and Cruden, D.M. 2005. Probabilistic assessment of stability of a cut slope in residual soil. Géotechnique **55**(1): 77-84.

Escario, V., and Saez, J. 1986. The shear strength of partly saturated soils. Géotechnique **36**(3): 453-456.

Fenton, G.A., and Griffiths, D.V. 2005. A slope stability reliability model. *In* Proceedings of the K.Y. Lo Symposium, London, Ontario.

Fenton, G.A., and Griffiths, D.V. 2008. Risk assessment in geotechnical engineering. 1st ed. John Wiley & Sons, Hoboken, New Jersey. pp. 461.

Fredlund, D.G., Morgenstern, N.R., and Widger, R.A. 1978. The shear strength of an unsaturated soil. Canadian Geotechnical Journal **15**(3): 313-321.

Gan, J.K., Fredlund, D.G., and Rahardjo, H. 1988. Determination of the shear strength parameters of an unsaturated soil using the direct shear test. Canadian Geotechnical Journal **25**(3): 500-510.

Gavin, K., and Xue, J. 2009. Use of a genetic algorithm to perform reliability analysis of unsaturated soil slopes. Geotechnique **59**(6): 545-549. doi: 10.1680/geot.8.T.004.

Griffiths, D.V., and Fenton, G.A. 1993. Seepage beneath water retaining structures founded on spatially random soil. Geotechnique **43**(4): 577-587.

Griffiths, D.V., and Fenton, G.A. 2004. Probabilistic Slope Stability Analysis by Finite Elements. Journal of Geotechnical and Geoenvironmental Engineering **130**(5): 507-518.

Griffiths, D.V., Huang, J., and Fenton, G.A. 2011. Probabilistic infinite slope analysis. Computers and Geotechnics **38**(4): 577-584. doi: 10.1016/j.compgeo.2011.03.006.

Griffiths, D.V., Huang, J.S., and Fenton, G.A. 2009. Influence of Spatial Variability on Slope Reliability Using 2-D Random Fields. Journal of Geotechnical and Geoenvironmental Engineering **135**(10): 1367-1378. doi: 10.1061/(asce)gt.1943-5606.0000099.

Griffiths, D.V., and Lane, P.A. 1999. Slope stability analysis by finite element. Géotechnique **49**(3): 387-403.

Griffiths, D.V., and Lu, N. 2005. Unsaturated slope stability analysis with steady infiltration or evaporation using elasto-plastic finite elements. International Journal for Numerical and Analytical Methods in Geomechanics **29**: 249-267.

Hicks, M.A., Chen, J., and Spencer, W.A. 2008. Influence of spatial variability on 3D slope failures. *In* Proceedings of 6th International Conference on Computer Simulation in Risk Analysis and Hazard Mitigation. *Edited by* C.A. Brebbia and E. Beriatos, Thessaly, Greece. pp. 335-342.

Hicks, M.A., and Samy, K. 2002. Influence of heterogeneity on undrained clay slope stability. Quarterly Journal of Engineering Geology and Hydrogeology **35**(1): 41−49.

Hicks, M.A., and Spencer, W.A. 2010. Influence of heterogeneity on the reliability and failure of a long 3D slope. Computer and Geotechnics **37**(7-8): 948-955.

Kozeny, J. 1927. Über kapillare Leitung des Wassers im Boden. Akad. Wiss. Wien **136**(2a): 271-306.

Lacasse, S., and Nadim, F. 1996. Uncertainties in charaterizing soil properties. *In* Uncertainty in the geologic environment. *Edited by* C. D. Shackelford and P.P. Nelson. ASCE, New York. pp. 49-75.

Le, T.M.H. 2011. Stochastic Modelling of Slopes and Foundations on Heterogeneous Unsaturated Soils. *In* School of Engineering. The University of Glasgow, Glasgow, UK. p. 342.

Le, T.M.H., Eiksund, G., and Strøm, P.J. 2013a. Statistical characterisation of soil porosity. *In* Proceeding of the 11th In International Conference on Structural Safety & Reliability. *Edited by* G. Deodatis and B. Ellingwood and D. Frangopol. CRC Press/Balkema, Columbia University, New York, USA.

Le, T.M.H., Gallipoli, D., Sanchez, M., and Wheeler, S.J. 2012. Stochastic analysis of unsaturated seepage through randomly heterogeneous earth embankments. International Journal for Numerical and Analytical Methods in Geomechanics **36**(8): 1056-1076. doi: 10.1002/nag.1047.

Le, T.M.H., Gallipoli, D., Sanchez, M., and Wheeler, S.J. 2013b. Rainfall-induced differential settlements of foundations on heterogeneous unsaturated soils. Geotechnique. doi: http://dx.doi.org/10.1680/geot.12.P.181.

Leij, F.J., Alves, W.J., van Genuchten, M.T., and Williams, J.R. 1996. The UNSODA Unsaturated Soil Hydraulic Database User's Manual, version 1.0.

Li, K.S., and Lumb, P. 1987. Probabilistic design of slopes. Canadian Geotechnical Journal **24**: 520-531.

Low, B.K., and Tang, W.H. 1997. Reliability analysis of reinforced embankments on soft ground. Canadian Geotechnical Journal **34**(5): 672-685.

Lu, N., and Godt, J. 2008. Infinite slope stability under steady unsaturated seepage conditions. Water Resources Research **44**. doi: W11404, doi:10.1029/2008WR006976.

Lumb, P. 1974. Application of statistics in soil mechanics. *In* Soil mechanics: New horizons. *Edited by* I.K. Lee. Butterworth's, London.

Matsuo, M., and Kuroda, K. 1974. Probabilistic approach to the design of embankments. Soils and Foundations **14**(1): 1-17.

Mostyn, G.R., and Li, K.S. 1993. Probabilistic slope analysis: state-of-play. *In* Proceedings of the conference on probabilistic methods in geotechnical engineering, Canberra, Australia. pp. 89-109.

Mostyn, G.R., and Soo, S. 1992. The effect of autocorrelation on the probability of failure of slopes. *In* Proceedings of 6th Australia, New Zealand Conference on Geomechanics: Geotechnical Risk. pp. 542-546.

Ng, C.W.W., and Shi, Q. 1998. A numerical investigation of the stability of unsaturated soil slopes subjected to transient seepage. Computers and Geotechnics **22**(1): 1-28.

Onyejekwe, S., and Ge, L. 2013. Scale of Fluctuation of Geotechnical Parameters Estimated from CPTu and Laboratory Test Data. *In* Foundation Engineering in the Face of Uncertainty. *Edited by* J.L. Withiam and K.-K. Phoon and M. Hussein. American Society of Civil Engineers, Geo-Congress 2013, San Diego, Californita. pp. 434-443.

Phoon, K., and Kulhawy, F. 1999. Characterization of geotechnical variability. Canadian Geotechnical Journal(36): 612-624.

Phoon, K., Santoso, A., and Quek, S. 2010. Probabilistic Analysis of Soil-Water Characteristic Curves. Journal of Geotechnical and Geoenvironmental Engineering **136**(3): 445-455. doi: doi:10.1061/(ASCE)GT.1943-5606.0000222.

Phoon, K.K., Nadim, F., Uzielli, M., and Lacasse, S. 2006. Soil variability analysis for geotechnical practice. *In* Characterisation and Engineering Properties of Natural Soils, Two Volume Set. Taylor & Francis.

Rodríguez, R., Sánchez, M., Lloret, A., and Ledesma, A. 2007. Experimental and numerical analysis of a mining waste desiccation. Canadian Geotechnical Journal **44**: 644-658.

Santoso, A., Phoon, K.K., and Quek, S.T. 2011a. Probability Models for SWCC and Hydraulic Conductivity. *In* Proceedings, Fourteenth Asian Regional Conference on Soil Mechanics and Geotechnical Engineering (14ARC), Hong Kong, China.

Santoso, A.M., Phoon, K.-K., and Quek, S.-T. 2011b. Effects of soil spatial variability on rainfall-induced landslides. Computers and Structures **89**(11–12): 893-900. doi: 10.1016/j.compstruc.2011.02.016.

Tsaparas, I., Rahardjo, H., Toll, D.G., and Leong, E.C. 2002. Controlling parameters for rainfall-induced landslides. Computers and Geotechnics **29**(1): 1-27.

UPC. 2010. CODE_BRIGHT User's Guide: A 3-D program for thermo-hydro-mechanical analysis in geological media. Cent. Int. de Metodos Numericos en Ing. Univ. Politecnica de Catalunya, Department of Geotechnical Engineering and Geosciences, Barcelona, Spain.

van Genuchten, M.T. 1980. A closed form equation for predicting the hydraulic conductivity of unsaturated soils. Soil Science Society of America Journal **44**: 892-898.

van Genuchten, M.T., and Nielsen, D.R. 1985. On describing and predicting the hydraulic properties of unsaturated soils. Annales Geophysicae **3**(5): 615-627.

Zandarín, M.T., Oldecop, L.A., Rodríguez, R., and Zabala, F. 2009. The role of capillary water in the stability of tailing dams. Engineering Geology **105**: 108-118.

Zhang, J., Huang, H.W., Zhang, L.M., Zhu, H.H., and Shi, B. 2014. Probabilistic prediction of rainfall-induced slope failure using a mechanics-based model. Engineering Geology **168**(0): 129-140. doi: http://dx.doi.org/10.1016/j.enggeo.2013.11.005.

Zhang, L.L., Zhang, L.M., and Tang, W.H. 2005. Technical note: Rainfall-induced slope failure considering variability of soil properties. Géotechnique **55**(2): 183-188.

Zhu, T. 2014. Some Useful Numbers on the Engineering Properties of Materials -GEOL 615 Course note Available from http://www.stanford.edu/~tyzhu/Documents/Some%20Useful%20Numbers.pdf [accessed 23 May 2014].

Zienkiewicz, O.C., Taylor, R.L., and Zhu, J.L. 2005. The finite element method: Its basis and fundamentals. Fifth ed. McGraw-Hill, Oxford.

Table.1: Values of soil parameters

Hydraulic model			Mechanical model		
Symbol	Units	Value	Symbol	Units	Value
m		0.2	E	kPa x 10^3	100
η		5	v		0.3
ϕ_o		0.333	ϕ'	°	20
k_{so}	m/s	10^{-5}	c'	kPa	5
s_{eo}	kPa	20	ϕ^b	°	18

LIST OF FIGURE CAPTIONS

Fig.1. Slope geometry and boundary conditions (scale in metres).

Fig. 2. Comparison of *FoS* estimated using the LEM and the FEM (with the SRT) during and after the rainfall event.

Fig. 3. Variation of (a) degree of saturation and (b) unsaturated permeability with suction for different porosity values.

Fig. 4. A typical realization of ϕ (calculated from a random field of e with $\mu(e) = 0.5$, $COV_e = 0.8$, $\theta(e) = 8$ m). Point A indicates location of a sampling point to monitor displacement.

Fig. 5. Vertical displacements recorded during SRT analyses at different rainfall times (days) (corresponding to point A in Fig. 3).

Fig. 6. Pore water pressure contours and corresponding slip surface during and after rainfall (corresponding to the random porosity field in Fig. 4) ($\mu(e) = 0.5$, $COV_e = 0.8$, $\theta(e) = 8$ m).

Fig. 7. Convergence of (a, b) $\mu(FoS)$ and (c, d) $\mu(A_s)$ with N (example from the Monte Carlo simulation with $\mu(e)= 0.5$, $COV_e = 0.8$, $\theta(e) = 8$ m).

Fig. 8. Histograms (bars) with fitted log-normal distributions (continuous line) of *FoS* and A_s at different times (example from the Monte Carlo simulation with $\mu(e)= 0.5$, $COV_e = 0.8$, $\theta(e) = 8$ m).

Fig. 9. Variation of $\mu(\text{FoS})$ and COV_{FoS} over time for various (a,b) COV_e (with $\mu(e) = 0.5$, $\theta(e) = 8$ m) (c,d) $\theta(e)$ (with $\mu(e) = 0.5$, $COV_e = 0.8$) (e,f) α (with $\mu(e) = 0.5$, $COV_e = 0.8$).

Fig. 10. Probability of failure P_f against (a) COV_e (b) $\theta(e)$ at different times.

Fig.11. Variation of $\mu(A_s)$ and COV_{As} over time for (a,b) various COV_e ($\mu(e) = 0.5$, $\theta(e) = 8$ m) (c,d) various $\theta(e)$ ($\mu(e) = 0.5$, $COV_e = 0.8$) (e,f) α ($\mu(e) = 0.5$, $COV_e = 0.8$).

Fig. 12. Realisations (cross symbols) and contours of the bivariate normal distribution for *FoS* and A_s (lines) at 4 times during the rainfall period (example from the Monte Carlo simulation with $\mu(e) = 0.5$, $COV_e = 0.8$, $\theta(e) = 8$ m).

Fig. 13. Realisations (cross symbols) and contours of the bivariate normal distribution for *FoS* and A_s (lines) at 4 times during the post-infiltration period (example from the Monte Carlo simulation with $\mu(e) = 0.5$, $COV_e = 0.8$, $\theta(e) = 8$ m).

Fig. 14. Sample porosity distributions (calculated from the associated random fields of void ratio) corresponding to significantly different failure mechanisms: (a, c) large sliding mass with high values of *FoS* and (b, d) small sliding mass with low values of *FoS* (5 days, example from the Monte Carlo simulation with $COV_e = 0.8$ and $\theta(e) = 8$ m).

Fig. 15. Contour of 10% probability from bivariate normal probability at different times (indicated by numbers on the contours) on a quadrant plot (example from the Monte Carlo simulation with $\mu(e) = 0.5$, $COV_e = 0.8$, $\theta(e) = 8$ m).

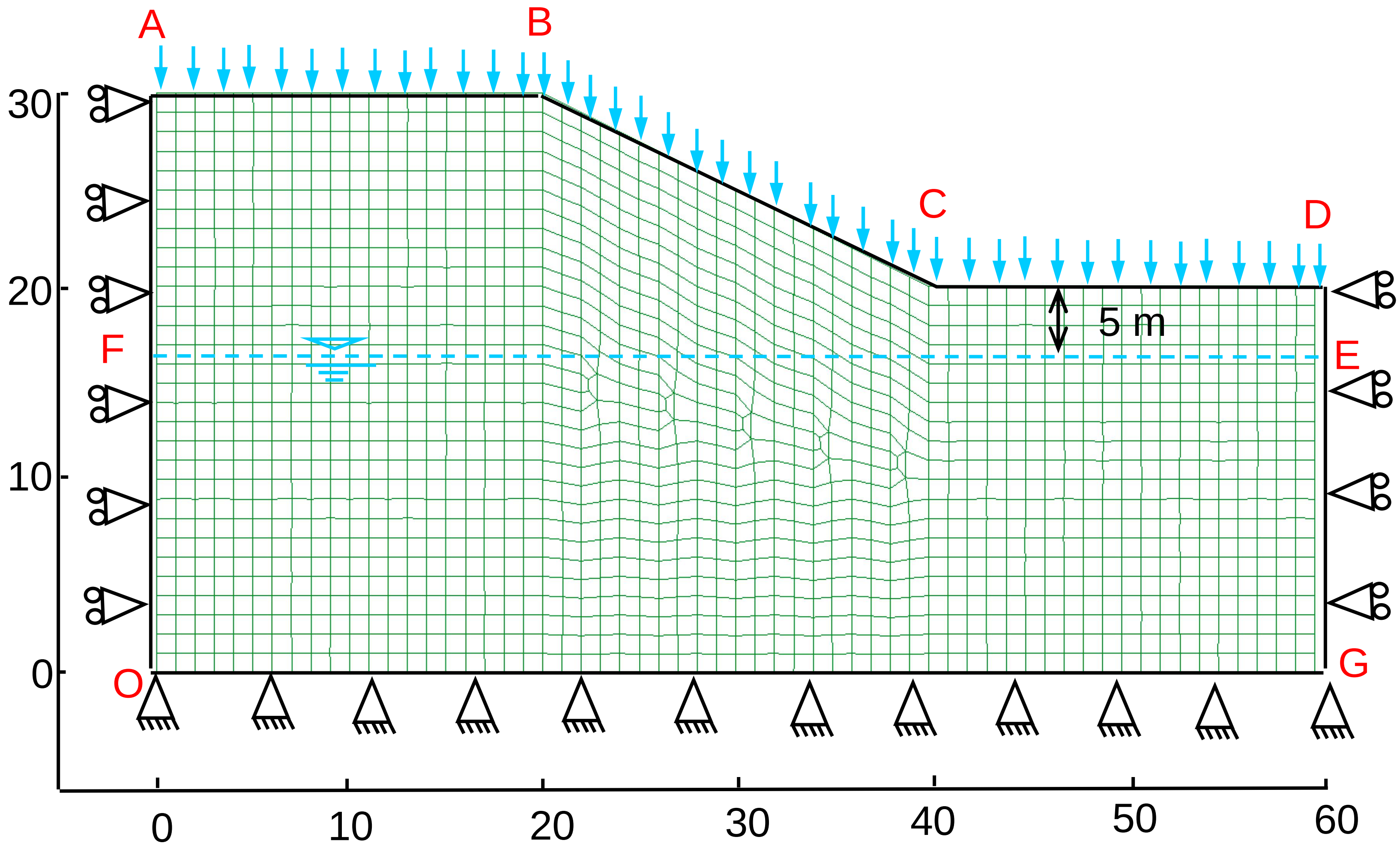
A
B
C
D
E
F
G
O
5 m
30
20
10
0
0
10
20
30
40
50
60

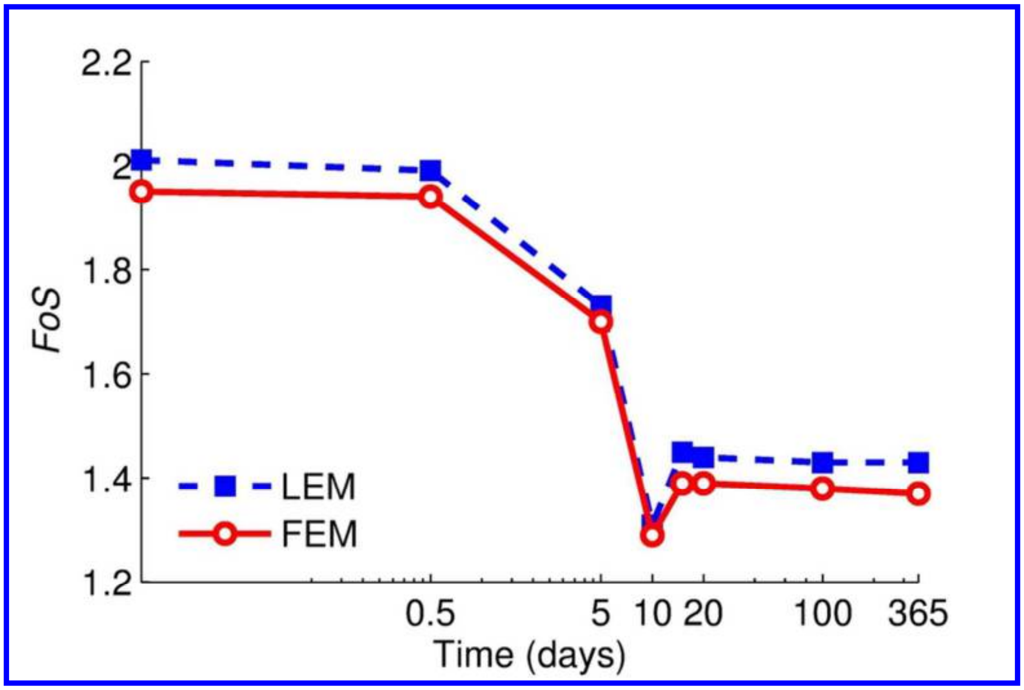

76x50mm (300 x 300 DPI)

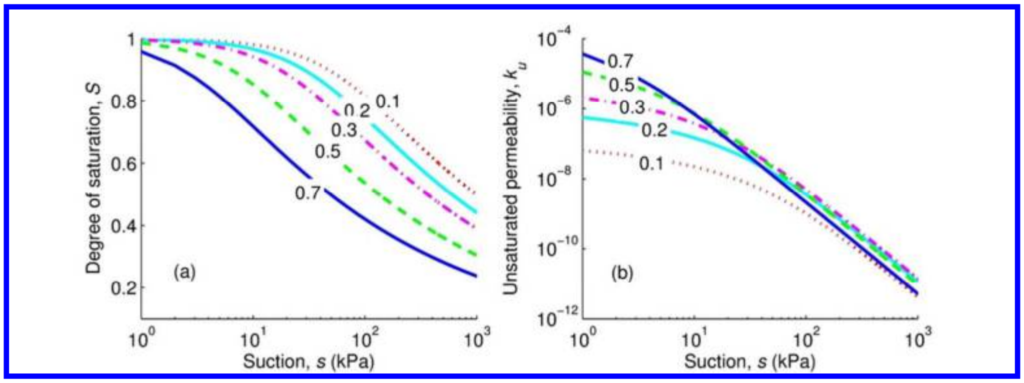

81x29mm (300 x 300 DPI)

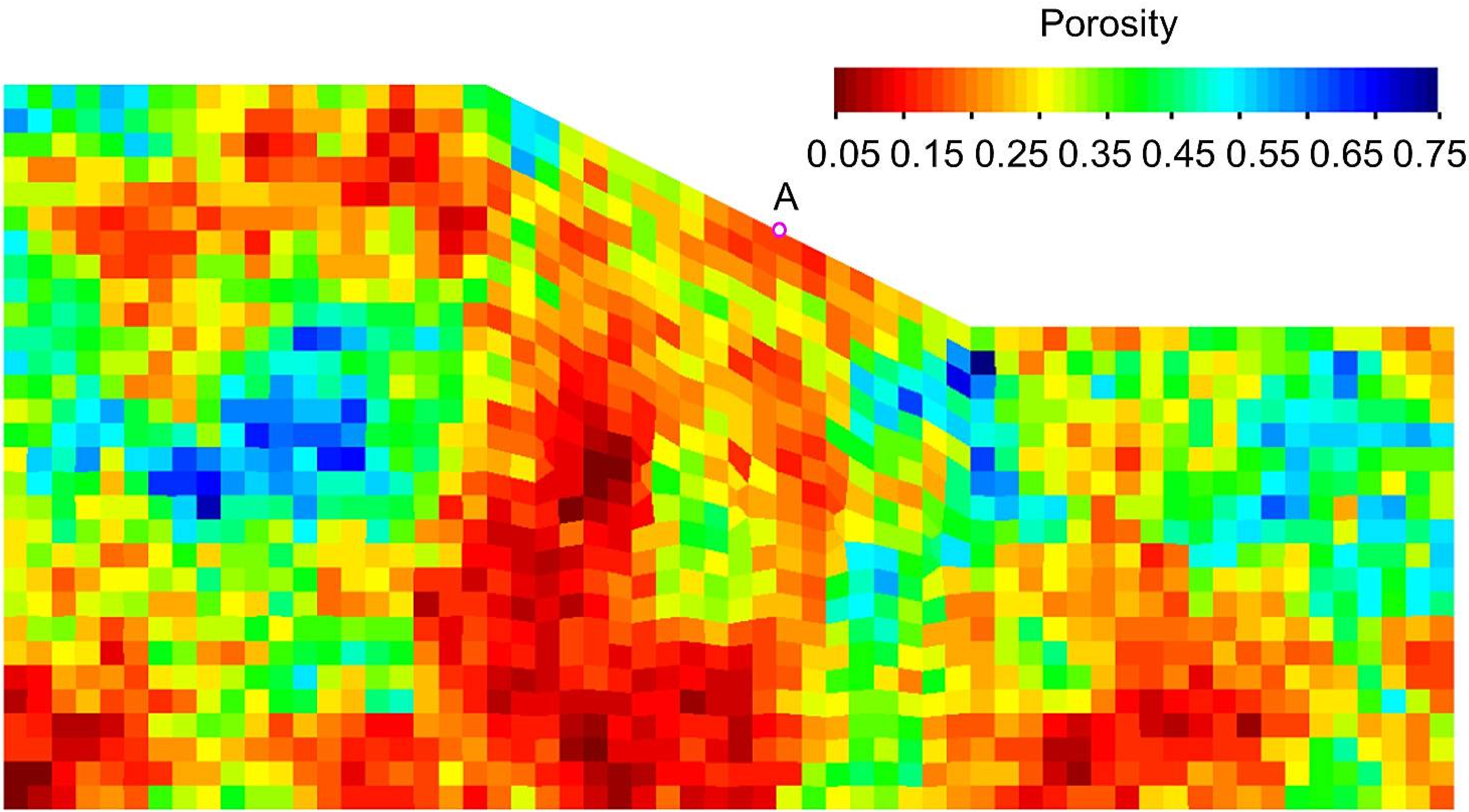
Porosity
0.05 0.15 0.25 0.35 0.45 0.55 0.65 0.75
A

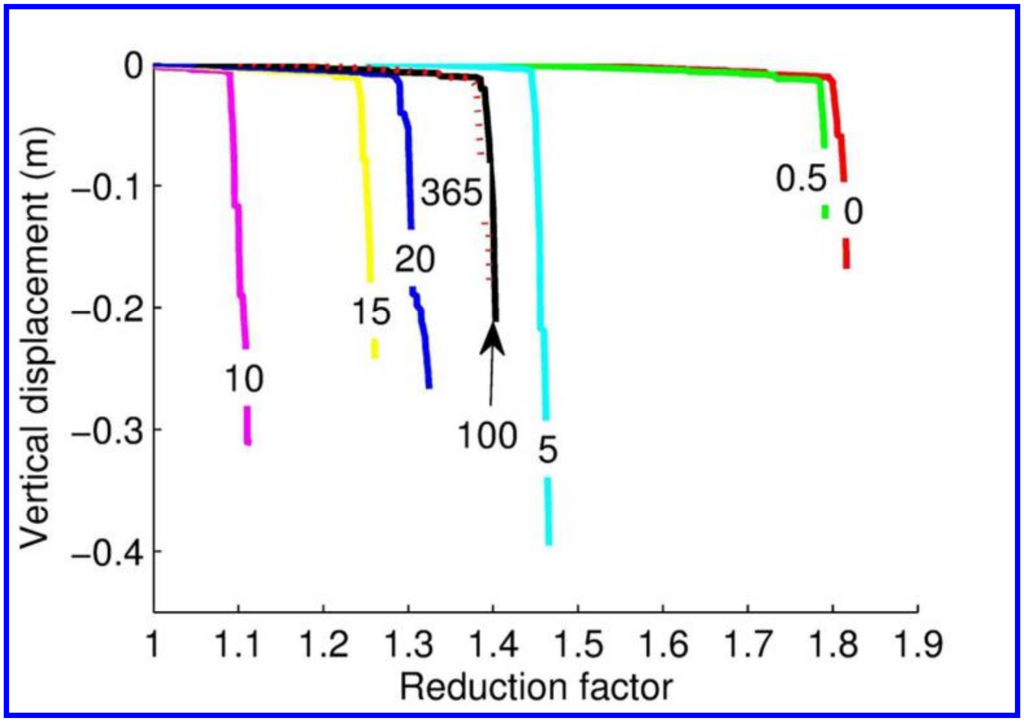

78x54mm (300 x 300 DPI)

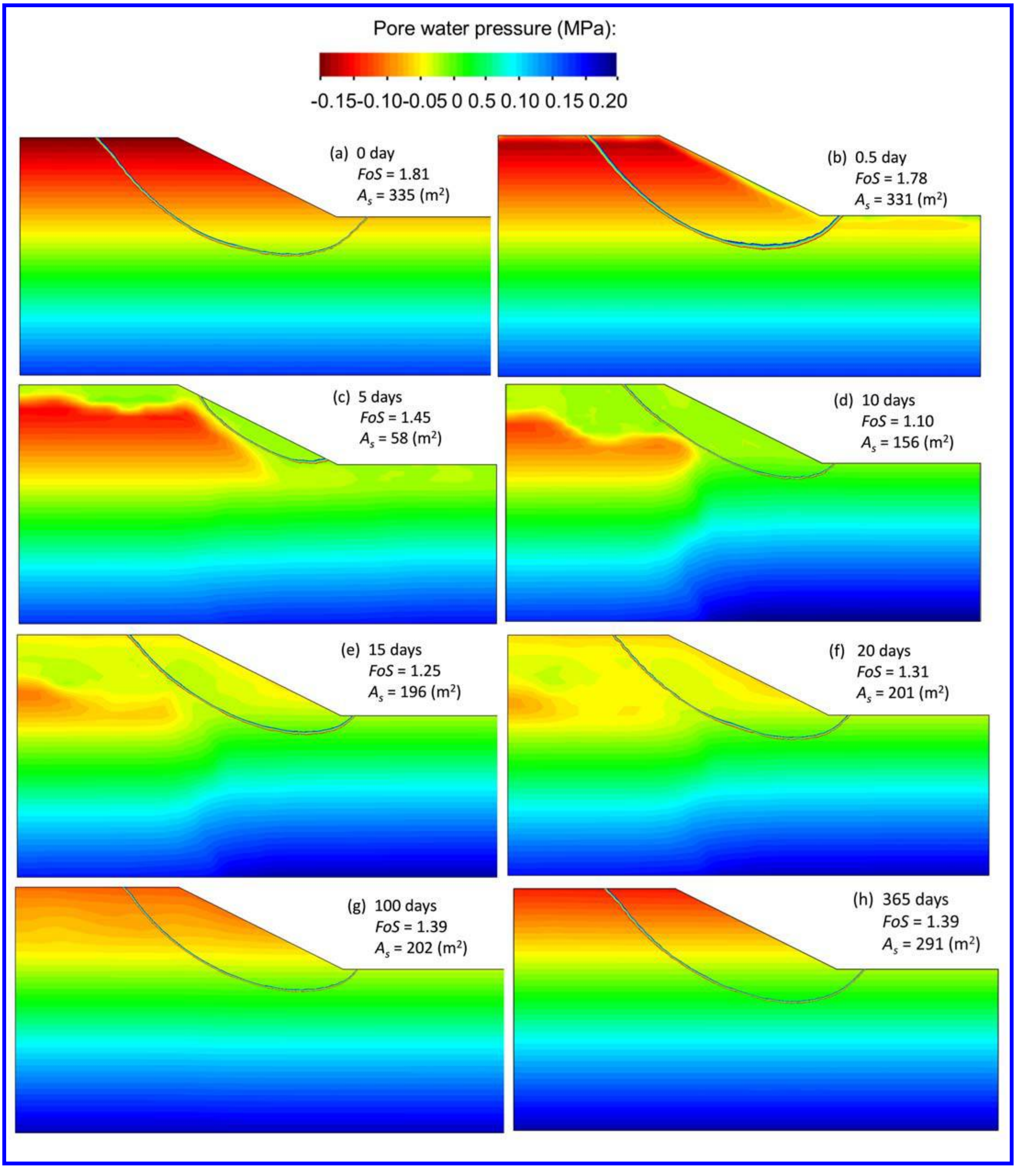
Pore water pressure (MPa):
-0.15 -0.10 -0.05 0 0.5 0.10 0.15 0.20
(a) 0 day
FoS = 1.81
As = 335 (m2)
(b) 0.5 day
FoS = 1.78
As = 331 (m2)
(c) 5 days
FoS = 1.45
As = 58 (m2)
(d) 10 days
FoS = 1.10
As = 156 (m2)
(e) 15 days
FoS = 1.25
As = 196 (m2)
(f) 20 days
FoS = 1.31
As = 201 (m2)
(g) 100 days
FoS = 1.39
As = 202 (m2)
(h) 365 days
FoS = 1.39
As = 291 (m2)

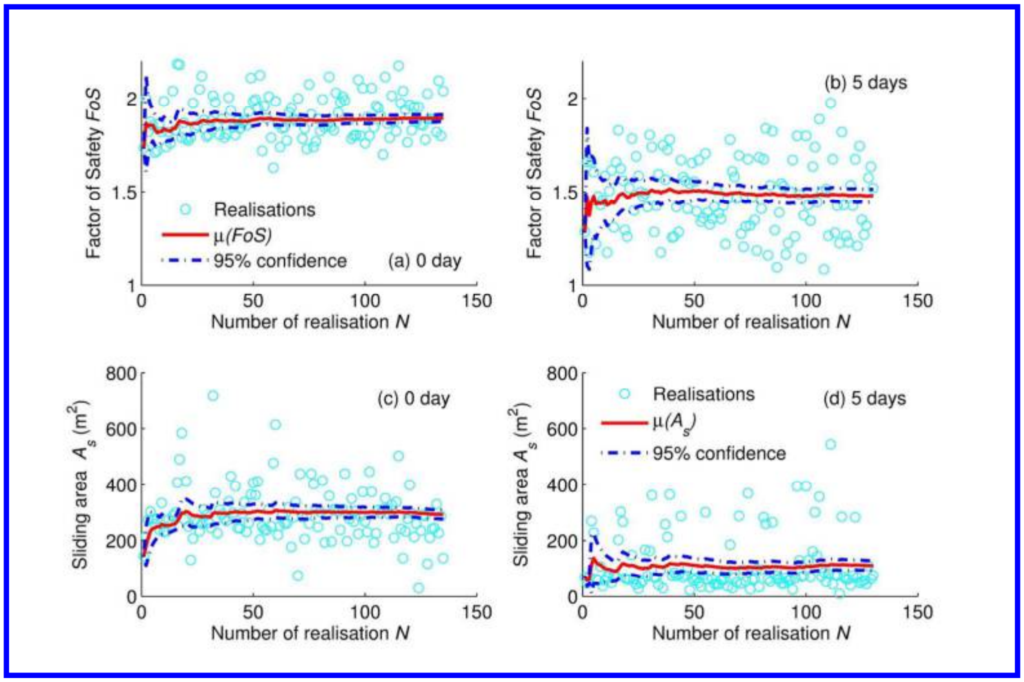

148x97mm (300 x 300 DPI)

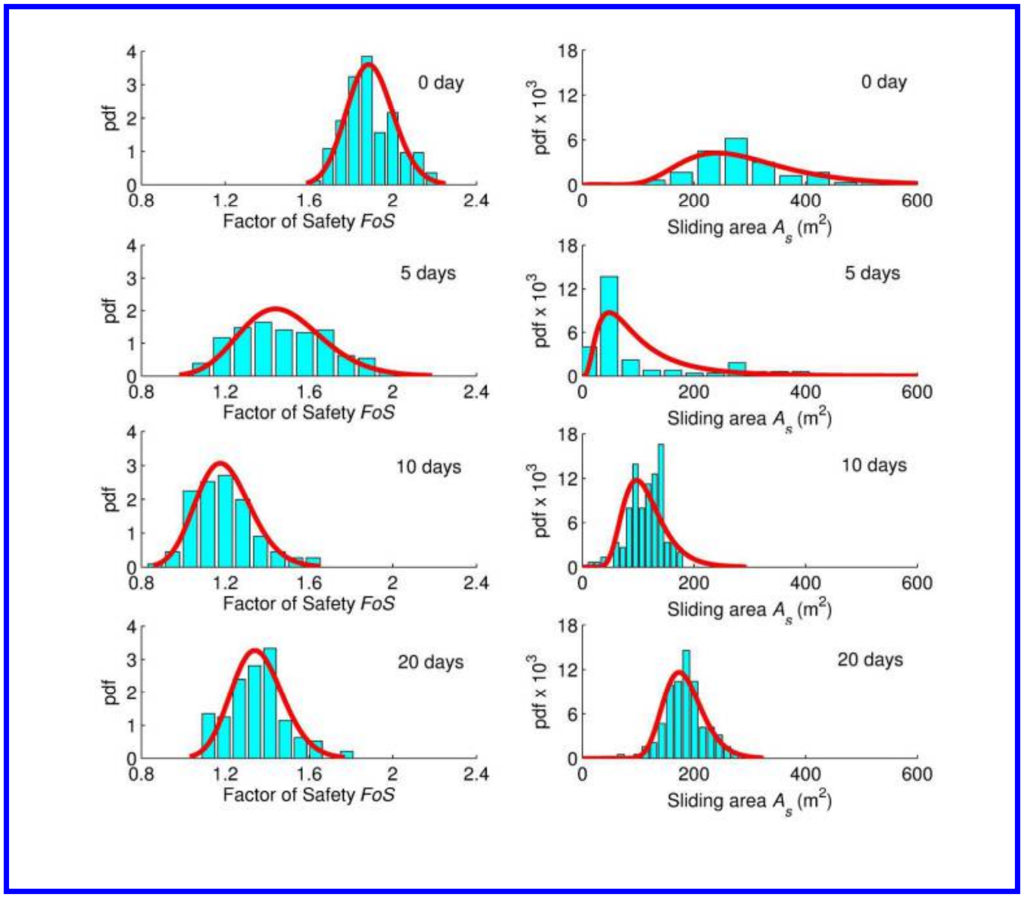

197x172mm (300 x 300 DPI)

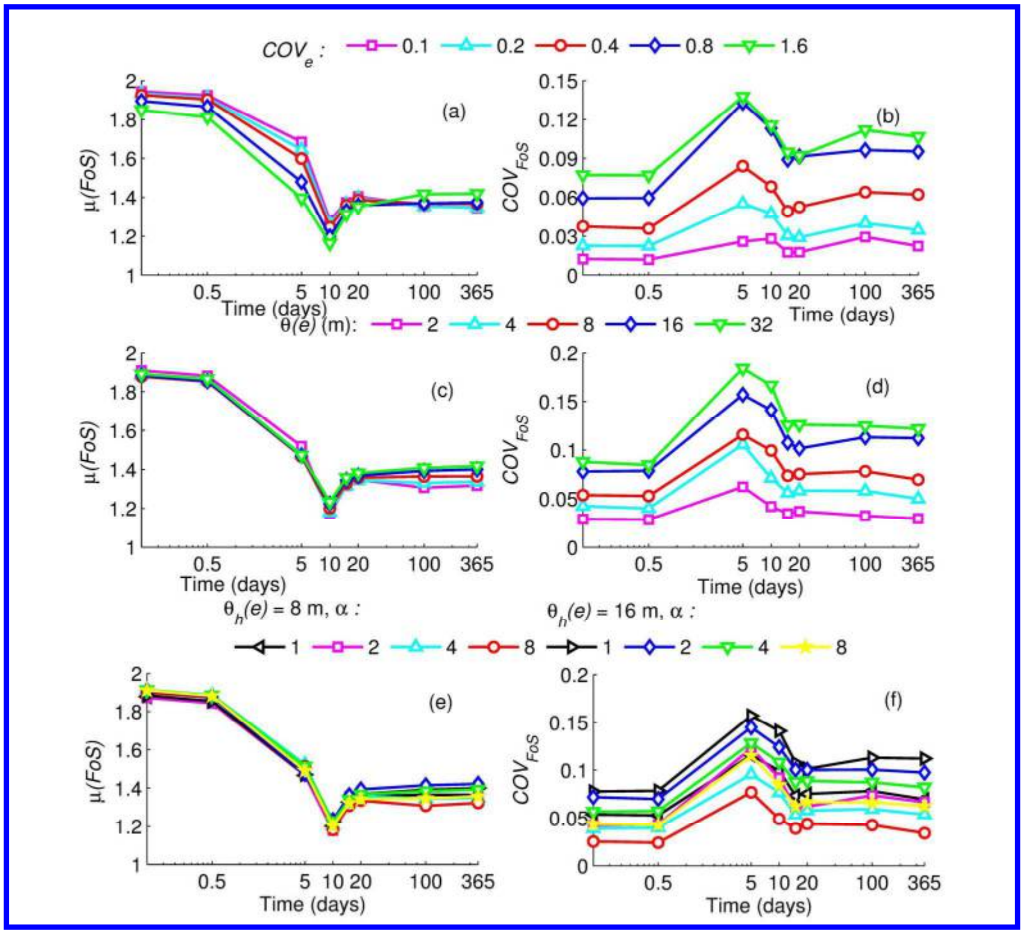

190x173mm (300 x 300 DPI)

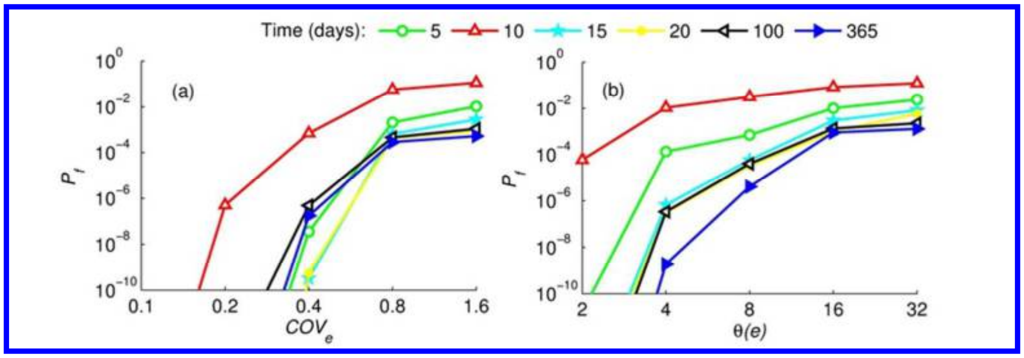

75x25mm (300 x 300 DPI)

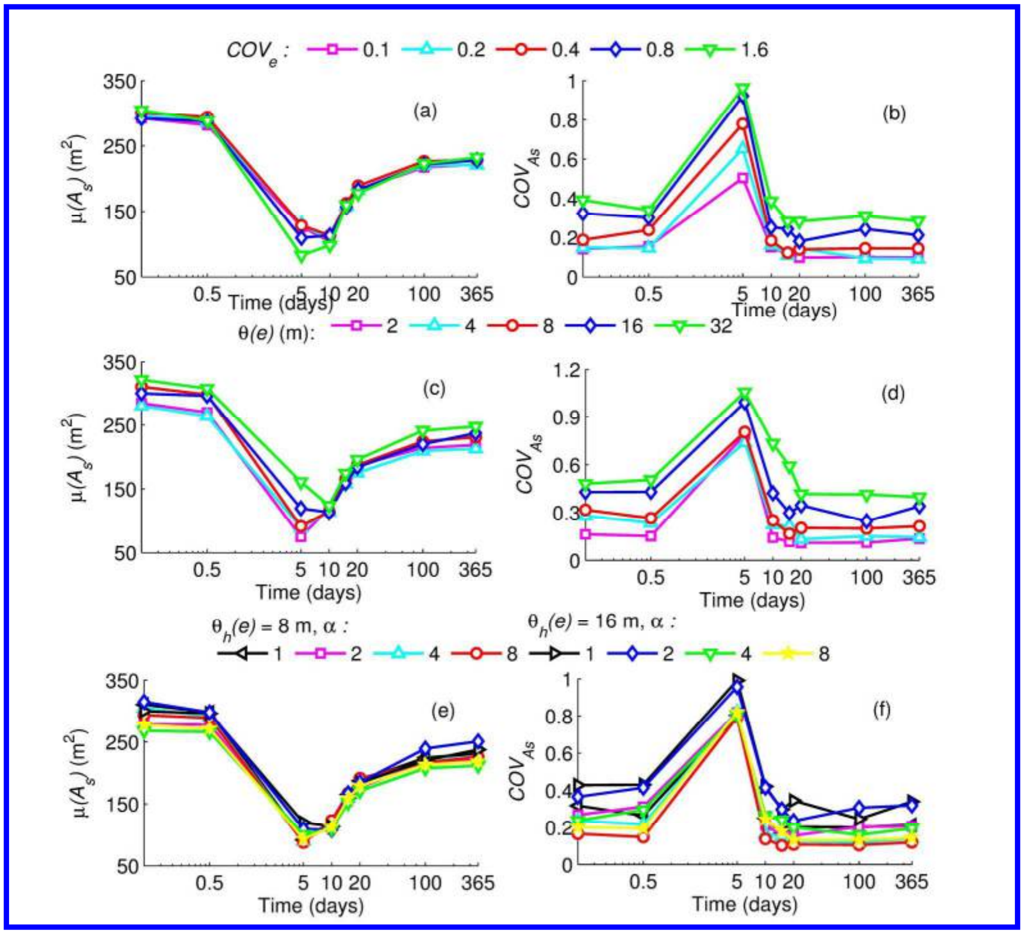

190x173mm (300 x 300 DPI)

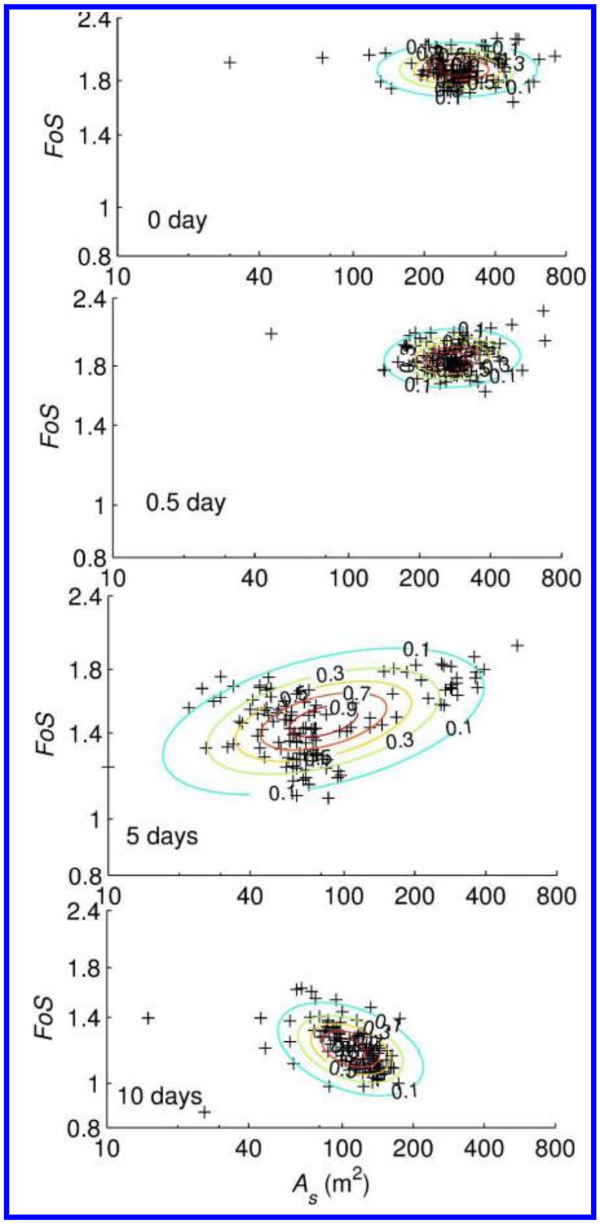

206x427mm (300 x 300 DPI)

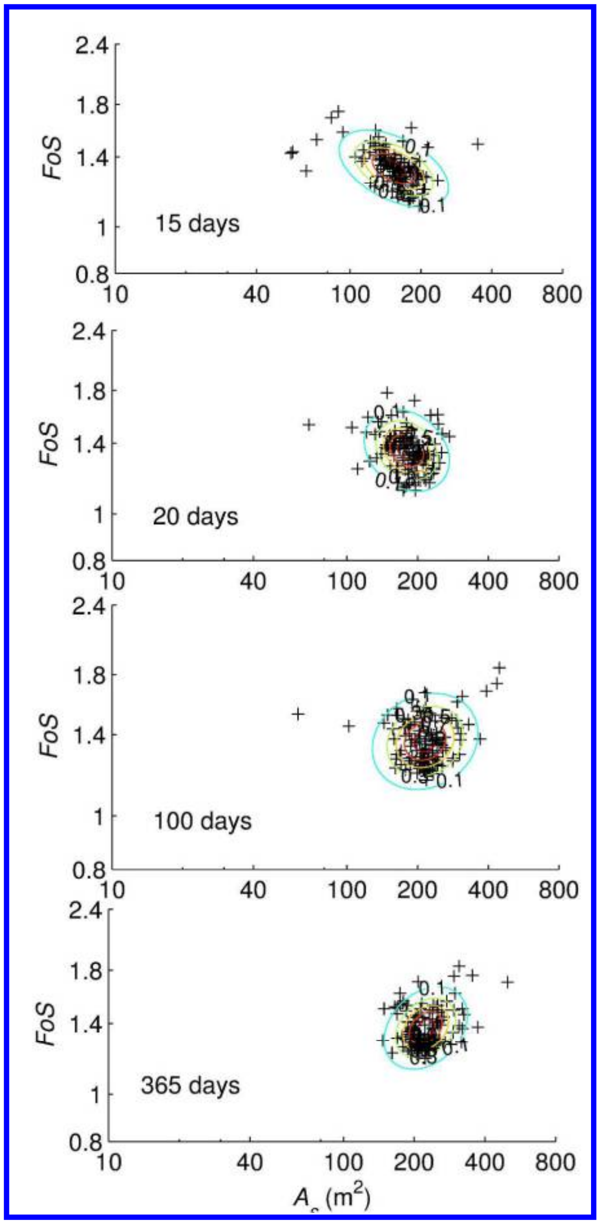

206x427mm (300 x 300 DPI)

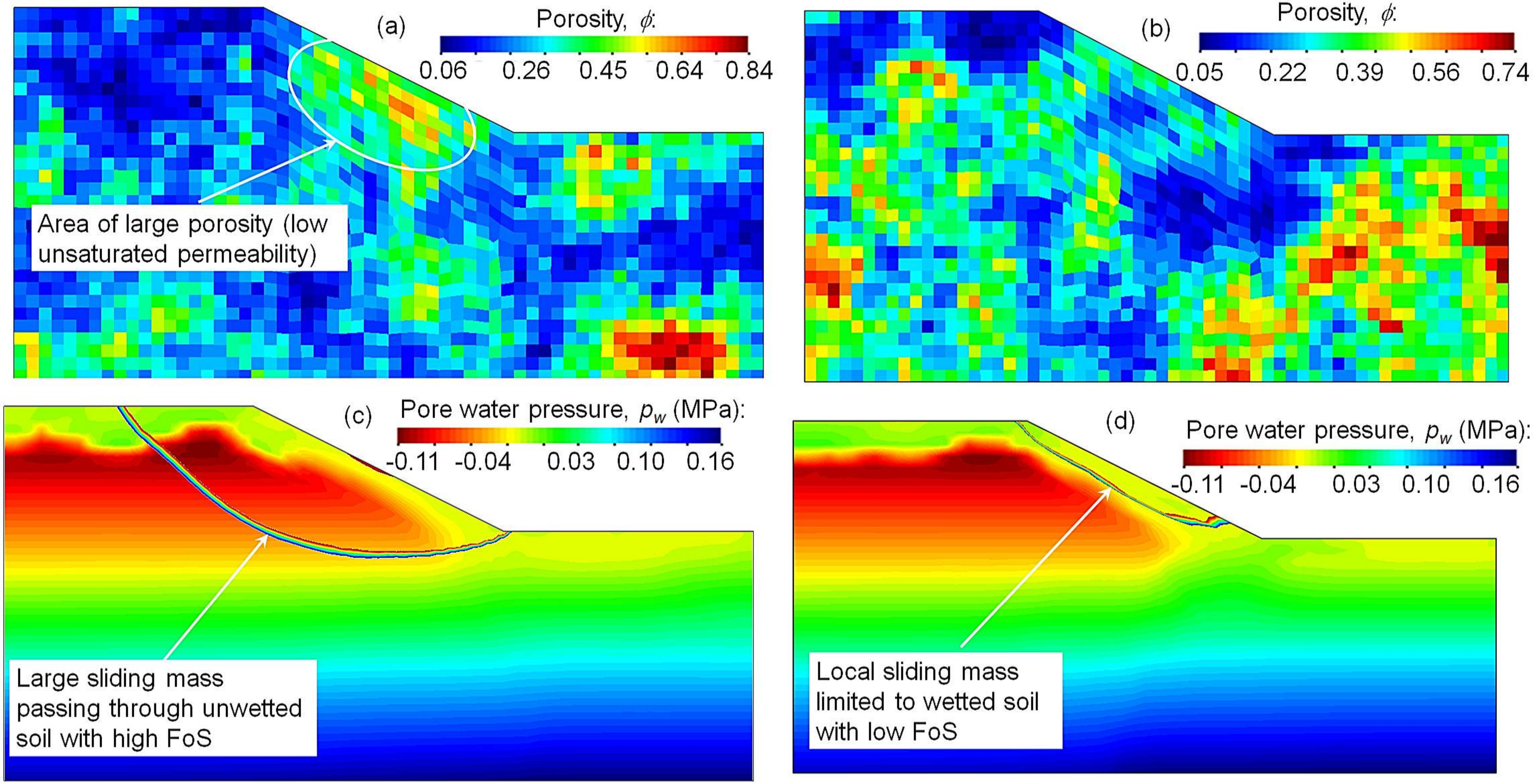
(a)
Porosity, ϕ:
0.06 0.26 0.45 0.64 0.84
Area of large porosity (low unsaturated permeability)
(b)
Porosity, ϕ:
0.05 0.22 0.39 0.56 0.74
(c)
Pore water pressure, p_w (MPa):
-0.11 -0.04 0.03 0.10 0.16
Large sliding mass passing through unwetted soil with high FoS
(d)
Pore water pressure, p_w (MPa):
-0.11 -0.04 0.03 0.10 0.16
Local sliding mass limited to wetted soil with low FoS

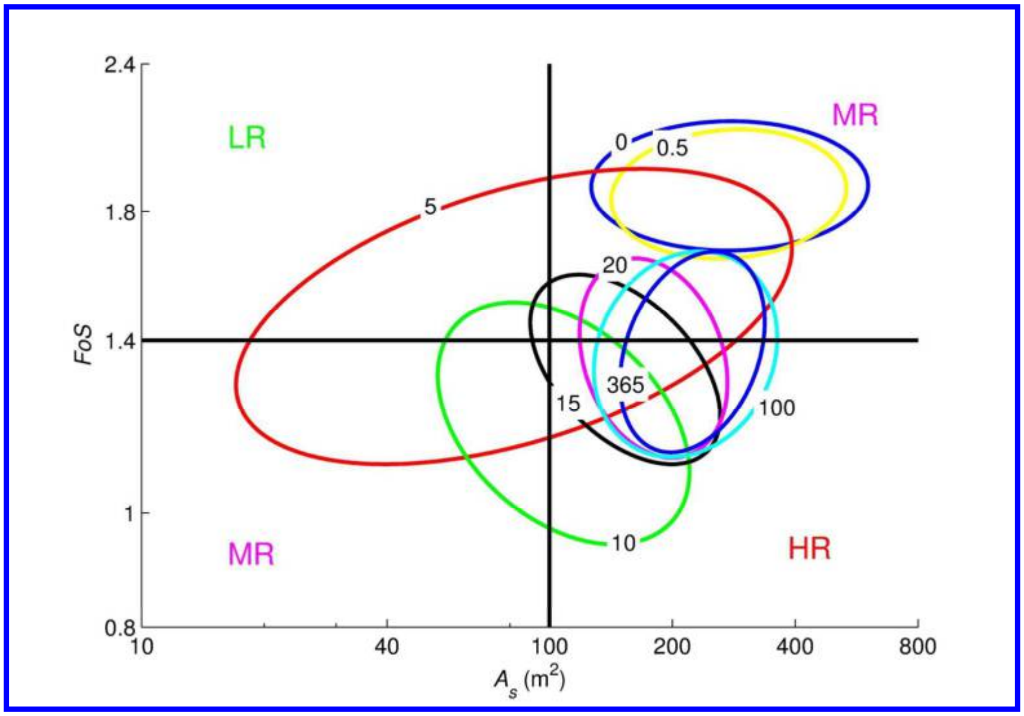

129x89mm (300 x 300 DPI)